



**STUDY OF MAGNETOGASDYNAMIC FLOW
ACCELERATION IN A SCRAMJET NOZZLE**

THESIS

Erik K. Ross, Ensign, USN

AFIT/GAE/ENY/05-J11

**DEPARTMENT OF THE AIR FORCE
AIR UNIVERSITY**

AIR FORCE INSTITUTE OF TECHNOLOGY

Wright Patterson Air Force Base, Ohio

Approved for public release; distribution unlimited

The views expressed in this thesis are those of the author and do not reflect the official policy or position of the United States Air Force, Department of Defense, or the United States Government.

AFIT/GAE/ENY/05-J11

STUDY OF MAGNETOGASDYNAMIC FLOW
ACCELERATION IN A SCRAMJET NOZZLE

THESIS

Presented to the Faculty of the
Department of Aeronautics and Astronautics
Graduate School of Engineering and Management
Air Force Institute of Technology
Air University
Air Education and Training Command
in Partial Fulfillment of the Requirements for the
Degree of Master of Science in Aeronautical Engineering

Erik K. Ross, B.S.

Ensign, USN

June, 2005

Approved for public release; distribution unlimited

STUDY OF MAGNETOGASDYNAMIC FLOW
ACCELERATION IN A SCRAMJET NOZZLE

Erik K. Ross, B.S.
Ensign, USN

Approved:

_____ Maj. Richard J. McMullan, Ph.D. Thesis Advisor	_____ Date
_____ Ralph A. Anthenien, Jr., Ph.D. Committee Member	_____ Date
_____ Jose Camberos, Ph.D. Committee Member	_____ Date

Abstract

The research project studied the benefits of Magnetogasdynamic (MGD) acceleration on a scramjet nozzle. MGD is a technology that relies on electromagnetic fields to extract and/or add energy to flow fields. The scramjet engine in the “AJAX” concept proposed by D.I.Brichkii et al. (2001) of St. Petersburg, Russia would utilize an MGD power generator in the diffuser which could potentially provide electrical power for the aircraft support systems and an MGD accelerator in the nozzle of the engine. Using an AFRL/VAAC CFD code that was modified for MGD computations, this project investigated the effect conductivity and load factor had on the specific thrust and efficiency of an MGD accelerator composed of segmented electrodes in the nozzle of a scramjet engine. For a load factor of 1.6, results showed a 95% increase in specific thrust. When MGD generation was employed at a load factor of 0.8, a 31% decrease in specific thrust was calculated. The solutions included high wall temperatures which need more investigation for MGD acceleration to be practical.

Acknowledgements

I am grateful for all of Major McMullan's help throughout the project. Without his patience and guidance I would not have been able to accomplish my thesis in only a year. I would like to thank Dr. Camberos, Major Lindsey, and Captain Earp for their help throughout the beginning of the project in understanding MGD. I would like to thank Captain Earp for the reference material on MHD. I appreciate the work of Dr. Gaitonde and all of AFRL including Barry Crocker who helped me with LaTeX. I recognize Dr. John Schmisser of AFOSR/NA for the funding support for this research. I would like to recognize the CFD Applications course taught by Lieutenant Colonel Maple early in the IGEP year. Also, I thank all my fellow Ensigns for their help throughout the year.

Erik K. Ross

Table of Contents

	Page
Abstract	iv
Acknowledgements	v
List of Figures	viii
List of Tables	x
List of Symbols	xi
List of Abbreviations	xv
1. Introduction	1-1
1.1 Scramjet Research	1-2
1.2 Magnetogasdynamics	1-3
1.3 Current Research	1-5
2. Governing Equations	2-1
2.1 Navier-Stokes Equations	2-1
2.1.1 Ideal Gas Law	2-2
2.1.2 Vector Form of the Navier-Stokes Equations	2-2
2.2 Special Relativity	2-4
2.2.1 Reference Frames	2-4
2.2.2 Lorentz Transformations	2-4
2.3 Maxwell Equations	2-5
2.3.1 Ohm's Law	2-5
2.3.2 Constitutive Relations	2-6
2.3.3 Magnetogasdynamic Assumptions	2-7

	Page
2.3.4 Maxwell's Equations for Magnetogasdynamic Flow	2-8
2.4 Magnetogasdynamic Equations	2-8
2.4.1 Non-dimensionalizing the Magnetogasdynamic Equations	2-9
3. Computational Set-Up	3-1
3.1 MGD 3-D Computational Code	3-1
3.2 Thrust Calculation Model	3-1
3.3 Efficiency Computation Model	3-2
3.4 Computational Domain	3-5
3.5 Computational Parameters	3-6
3.6 Computational Cases	3-10
4. Results	4-1
4.1 Specific Thrust	4-1
4.2 Baseline Flow field	4-5
4.3 Acceleration Case, $\mathcal{K} = 1.6$	4-7
4.4 Generation, $\mathcal{K} = 0.8$	4-13
4.5 Efficiency	4-17
5. Conclusions	5-1
5.1 This Study	5-1
5.2 Future Work	5-3
Appendix A. Other Cases	A-1
Bibliography	BIB-1
Vita	VITA-1

List of Figures

Figure		Page
1.1.	University of Queensland’s HyShot[19].	1-2
1.2.	NASA’s X-43A[25].	1-4
1.3.	The “AJAX” concept[9].	1-5
1.4.	The Direction of the Lorentz Force.	1-6
1.5.	Simplified Mach 8 scramjet model design[10]	1-7
3.1.	Diagram of electrodes.	3-4
3.2.	Three dimensional MGD accelerator geometry.	3-6
3.3.	Three dimensional conductivity pattern 1.	3-8
3.4.	Three dimensional conductivity pattern 2.	3-9
4.1.	Specific Thrusts	4-2
4.2.	Stream Thrust Function for Conductivity 1	4-2
4.3.	Stream Thrust Function for Conductivity 2	4-3
4.4.	Mach Number Contours for Baseline Case	4-5
4.5.	Temperature Contours for Baseline Case	4-6
4.6.	Pressure Contours for Baseline Case	4-6
4.7.	K16 Lorentz Force Vectors (top: x-z midplane, bottom: x-y mid- plane)	4-7
4.8.	K16 Mach Number Contours	4-8
4.9.	K16 Electric Field Vectors (top: x-z midplane, bottom: x-y mid- plane)	4-9
4.10.	K16 Electric Potential Contours	4-10
4.11.	K16 Temperature (top: x-z midplane, bottom: x-y midplane)	4-11
4.12.	Close up of K16 Temperature	4-12
4.13.	K08 Lorentz Force Vectors (top: x-z midplane, x-y midplane)	4-14

Figure		Page
4.14.	K08 Mach Number Contours	4-14
4.15.	K08 Electrical Field Vectors (top: x-z midplane, x-y midplane)	4-15
4.16.	K08 Pressure Contours	4-16
4.17.	K08 Temperature Contours (top: x-z midplane, bottom: x-y midplane)	4-16
4.18.	Accelerator Pseudo Efficiency	4-17
4.19.	Accelerator Projected Efficiency	4-18
A.1.	K09 $\vec{j} \times \vec{B}$	A-1
A.2.	K09 Mach Number	A-1
A.3.	K12 $\vec{j} \times \vec{B}$	A-2
A.4.	K12 Mach Number	A-2
A.5.	K14 $\vec{j} \times \vec{B}$	A-3
A.6.	K14 Mach Number	A-3
A.7.	K08_SIG2 $\vec{j} \times \vec{B}$	A-4
A.8.	K08_SIG2 Mach Number	A-4
A.9.	K09_SIG2 $\vec{j} \times \vec{B}$	A-5
A.10.	K09_SIG2 Mach Number	A-5
A.11.	K12_SIG2 $\vec{j} \times \vec{B}$	A-6
A.12.	K12_SIG2 Mach Number	A-6
A.13.	K14_SIG2 $\vec{j} \times \vec{B}$	A-7
A.14.	K14_SIG2 Mach Number	A-7
A.15.	K16_SIG2 $\vec{j} \times \vec{B}$	A-8
A.16.	K16_SIG2 Mach Number	A-8
A.17.	SIG1 Velocity	A-9
A.18.	SIG2 Velocity	A-9
A.19.	SIG1 Temperature	A-10
A.20.	SIG2 Temperature	A-10
A.21.	SIG1 Pressure	A-11
A.22.	SIG2 Pressure	A-11

List of Tables

Table		Page
3.1.	Freestream and MGD Accelerator Inlet Conditions.	3-7
3.2.	Dimensional Conversion Factors.	3-7
3.3.	Naming Scheme for Investigated Cases.	3-10
4.1.	Percent Difference in Specific Thrust, $\frac{F}{\dot{m}}$, from baseline case. . .	4-4

List of Symbols

Roman symbols:

A	area [m^2]
a	sound speed [$\frac{m}{s}$]
B	magnetic flux density [1]
B_0	magnitude of the magnetic flux density [T]
c_p	constant pressure specific heat [Pa]
D	electric flux density
E	electric field or viscous/inviscid component of the flux vector in the x - or ξ -direction [1]
E_0	magnitude of the applied electric field
\mathbf{E}	flux vector in the x - or ξ -direction
e	energy
F	force or viscous/inviscid component of the flux vector in the y - or η -direction
\mathbf{F}	flux vector in y - or η -direction
f	force density
G	viscous/inviscid component of the flux vector in the z - or ζ -direction
\mathbf{G}	flux vector in z - or ζ -direction
H	magnetic field
h	enthalpy
I	axial force function [N]
j	conduction current density [$\frac{A}{m^2}$]
\mathcal{K}	load factor
L	reference length [m]
\dot{m}	mass flow rate [$\frac{kg}{s}$]
M	Mach number [1]
Mm	magnetic Mach number

Pm	magnetic Prandtl number
Pr	Prandtl number
p	pressure [Pa]
\mathcal{Q}	interaction parameter [1]
q	heat flux
Re	Reynolds number
Rm	magnetic Reynolds number
S	source vector
Sa	mass flow rate specific thrust [m/s]
T	temperature [K]
t	time [s]
U	conservative variable vector
u	component of velocity in the x -direction
V	velocity
v	component of velocity in the y -direction
w	component of velocity in the z -direction
x	coordinate direction of the principle axis
y	coordinate direction of the principle axis
z	coordinate direction of the principle axis
ℓ	distance between the anode and a corresponding cathode [m]

Greek symbols:

ϵ	permittivity
γ	ratio of specific heats
κ	thermal conductivity
μ	permeability or viscosity
ν	kinematic viscosity
ρ	density
ρ_e	charge unit volume
σ	conductivity
τ	stress tensor
ϕ	electric potential
∂	partial differential operator
∇	gradient operator

Subscripts:

0	freestream value or reference location
e	electromagnetic
f	fluid
i	inviscid, index notation, or tensorial component
j, k	index notation or tensorial component
t	total condition
v	viscous
x	x-component or differentiation with respect to x
y	y-component or differentiation with respect to y
z	z-component or differentiation with respect to z

Superscripts:

'	rest frame
*	dimensionless quantity
\rightarrow	vector quantity
\rightarrow	vector quantity

Constants:

c	speed of light <i>in vacuum</i>	$2.998 \times 10^8 \frac{m}{s}$
\mathcal{R}	specific gas constant	$287 \frac{J}{kgK}$
$\epsilon_{0,e}$	electric constant (permittivity of free space)	$8.854 \times 10^{-12} \frac{F}{m}$
$\mu_{0,e}$	magnetic constant (permeability of free space)	$4\pi \times 10^{-7} \frac{H}{m}$

List of Abbreviations

Abbreviation		Page
CFD	... Computational Fluid Dynamics	1-1
scramjets	... Supersonic Combustion Ramjets	1-2
MGD	... Magnetogasdynamic	1-3
MPCE	... Magneto Plasma Chemical Engine	1-4
NSE	... Navier-Stokes Equations	2-1
LT	... Lorentz Transformations	2-4
ME	... Maxwell Equations	2-5
MLT	... Maxwell-Lorentz Transformations	2-6
MUSCL	... Monotone upstream-centered schemes for conservation	
laws	3-1

STUDY OF MAGNETOGASDYNAMIC FLOW ACCELERATION IN A SCRAMJET NOZZLE

1. Introduction

Since the Wright brother's first self powered flight on December 17, 1903[16], humans have achieved great advances in aviation. From the supersonic X-1 flown by Chuck Yeager on October 14, 1947[16] to Burt Rutan's 2005 X-Prize winning Space Ship One, the world is quickly getting smaller. The transportation industry counts down the days until a flight from New York to Tokyo only takes two hours[7, 2]. In this industry, speed is addictive.

Rockets and Ramjets have set the pace at Mach 6. However, these propulsion systems are limited by weight and drag; and new technologies are being investigated. In the designs prior to the X-1, the greatest limitation was structural. With airplanes falling apart as pilots attempted to break through the sound barrier, the process was primarily trial and error[16, 33]. At the expense of labor and lives, earlier advancements required deep pockets and long turnaround times. Today's engineering methods include ground testing and computational fluid dynamics (CFD) to explore new frontiers.

Sustained hypersonic flight has been that new frontier for over fifty years[16]. Current hypersonic propulsion systems include rocket and ramjet engines. However these systems have exhausted their speed potential. Rockets, though less susceptible to drag, are held back by the weight of the oxidizers that they must carry. Airbreathing ramjet propulsion eliminates the need for internal oxidizers.

Ramjets operate by slowing down the hypersonic flow to subsonic mach numbers for combustion[17]. Atmospheric oxygen is mixed with fuel and ignited. However, engine unstart can occur when too much fuel is introduced to the mixture. This increases the back pressure expelling the shock train from the inlet. Even with

proper fuel flow control, ramjets are not always effective. When approaching Mach 6, the process of slowing down the flow field creates too much drag for the thrust to overcome[24, 16, 2]. This is essentially the operational limitation that leads to the development of scramjets.

1.1 Scramjet Research

Supersonic combustion ramjets (scramjets) eliminate the limitations that are inherent in rockets and ramjets. Scramjets do not rely on internal oxidizers, nor do they require subsonic combustion[17]. However, there are significant challenges that must be met for the sustained hypersonic flight in the scramjet. Examples include engine unstart, and the fact that the scramjet, like the ramjet, needs a boost from an external supersonic propulsion system to get started[16, 2].



Figure 1.1 University of Queensland's HyShot[19].

The University of Queensland's HyShot Flight Program is one of several that has investigated scramjet propulsion. Their two flight dates were 30 Oct 2001 and 30 July 2002. Their next launch is scheduled for November 2005[19]. A picture of their scramjet engine and rocket stage is shown in Figure 1.1. The rocket was used to bring the scramjet up to 330 km. The rocket and scramjet engine were then directed

back down and the second rocket stage was fired. The scramjet then separated and propelled itself for 5 seconds at Mach 7.6 between 35 km and 23 km on hydrogen fuel[19, 16].

The Hyshot team had some difficulties unique to their design. Due to their vertical trajectory during the launch, accelerations reached a peak of 60g before decaying to 30g which could cause structural damage during the first second of flight [16, 19]. Recent ground tests and CFD studies at the University of Queensland show a promising revival of their design. Rated for Mach 10 conditions at 30 km in altitude, the HyShot team promises to beat the record of its competitor in November 2005[20].

NASA is The University of Queensland's main competitor. NASA's \$250 million X-43A Hyper-X has had two successful flights. Unlike the Australian HyShot, it incorporated the engine into the aircraft. This is done so that the underside of the fuselage provides external combustion before the inlet and external thrust surface after the nozzle. As shown in Figure 1.2, the X-43A is propelled by a Pegasus missile that is launched by a B-52 bomber. The first flight occurred on March 27, 2004 during which it reached Mach 7 at 100,000 ft[16, 34]. On its last flight it reached nearly Mach 10, or 7000 mph, as it flew at an altitude of 110,000 ft[25]. The current design has a few shortfalls. The X-43A is aerodynamically unstable, and the engine has a tendency to overheat[16]. This is coupled with the control problem of too much fuel getting into the combustor which increases back pressure and can eventually cause unstart[16, 2].

1.2 Magnetogasdynamics

In response to flow problems, some researchers have started investigating magnetogasdynamics (MGD) to control scramjet flow fields[16, 24, 7]. MGD is the study of electrically conducting gases. At velocities below Mach 9 at which sufficient spontaneous or thermal ionization does not occur[31], electron beams can be utilized to ionize the flow. MGD has been investigated for a variety of aerospace applications



Dryden Flight Research Center ED97 43968-04
B-52 CARRY-ALL: This artist's concept depicts the Hyper-X
research vehicle riding on a booster rocket prior to being launched
by Dryden Flight Research Center's B-52 at about 40,000 feet.

Figure 1.2 NASA's X-43A[25].

from boundary layer control around a reentry vehicle[29] to flow field acceleration in a nozzle.

Ohms law plays an intricate role in accelerating flow. The details of the law are discussed in Chapter 2. As an overview, the flow field can be accelerated with the addition of electrical energy to the flow, or it can be decelerated with the generation of electrical energy from the flow. One concept known as "AJAX" originated in St. Petersburg Russia with A. Kuranov and E. Sheikin at the Hypersonics Systems Research Institute[16] and involves both flow field acceleration and generation. Figure 1.3 shows a diagram of the "AJAX" concept. The Magneto-Plasma-Chemical Engine (MPCE), also referred to as a scramjet with MGD bypass, was developed

within its framework. The engine design incorporates an MGD generator that serves two purposes. It provides energy for the flight systems and an MGD accelerator which utilizes the Lorentz force vector in a direction that accelerates the flow field, and the generator serves as a means of reducing the flow velocity for combustion without significant pressure drop[16, 7, 14].

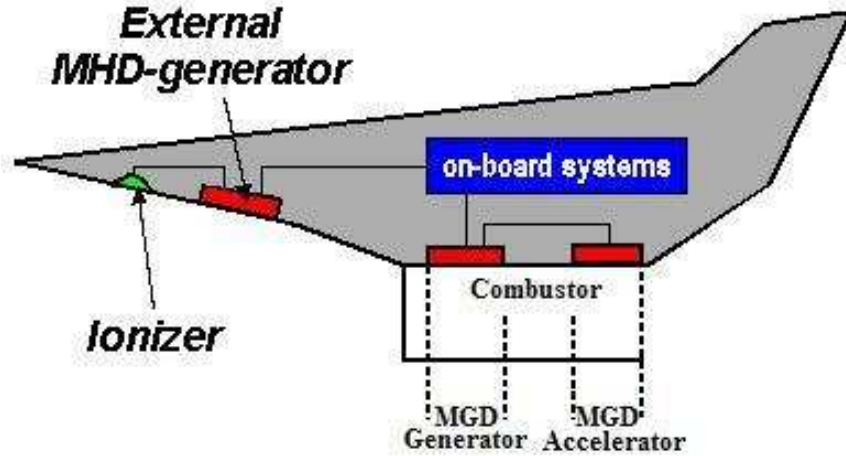


Figure 1.3 The “AJAX” concept[9].

The implementation of MGD is based on several conditions. These include method of ionization, and magnet and electrode placements. The flow can be ionized by injection of ionized particles or through use of an electron beam ionizer[11]. The electron beam ionizer is typically suggested since it produces the best current density to weight ratio to date[24].

The Lorentz force, or $\vec{j} \times \vec{B}$, is the driving force for MGD generation and acceleration in the scramjet. In order for this force to accelerate flow in the axial direction, the magnetic flux density, \vec{B} , and the current density, \vec{j} , must be perpendicular to the direction of flow, \vec{u} as shown in Figure 1.4 below.

1.3 Current Research

This thesis is part of a progressive effort to increase understanding of MGD flow control in a scramjet engine. The ultimate goal is to determine conditions required for

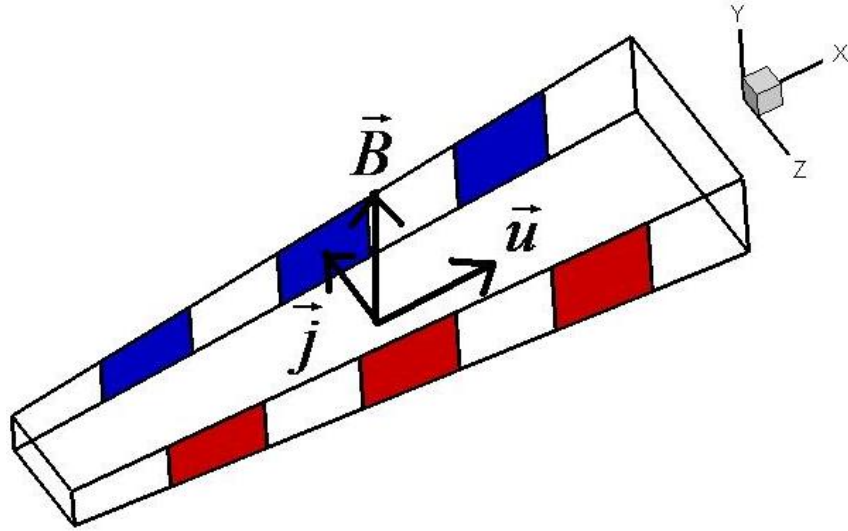


Figure 1.4 The Direction of the Lorentz Force.

a self-sustained scramjet engine that utilizes MGD generation to power its onboard electronics with enough power left over to accelerate the flow in the nozzle for added thrust. This particular study is focused on determining the conditions that improve efficiency.

Figure 1.5 shows the whole scramjet engine as proposed by Gaitonde[14]. This study investigates an accelerator with three electrodes as shown in Figure 1.4. The electrodes are the vertical plates on either side of the nozzle.

Harrington's work focused on flow field interaction and what parameters caused the greatest effects for continuous electrodes[16]. His work agreed with that of Gaitonde which stated that significant Joule heating effects at the electrodes made efficient flow field acceleration impractical for real implementations[16, 10]. However, their work also emphasized that an a study of efficiency should be performed.

The objective of this computational study was to address efficiency while also determining the effectiveness of differing conductivity pattern and load factor. Both acceleration and generation cases were considered.

With Maxwell's equations and Navier-Stokes equations serving as the cornerstone, the governing equations for MGD are summarized in Chapter 2. Then, Chapter

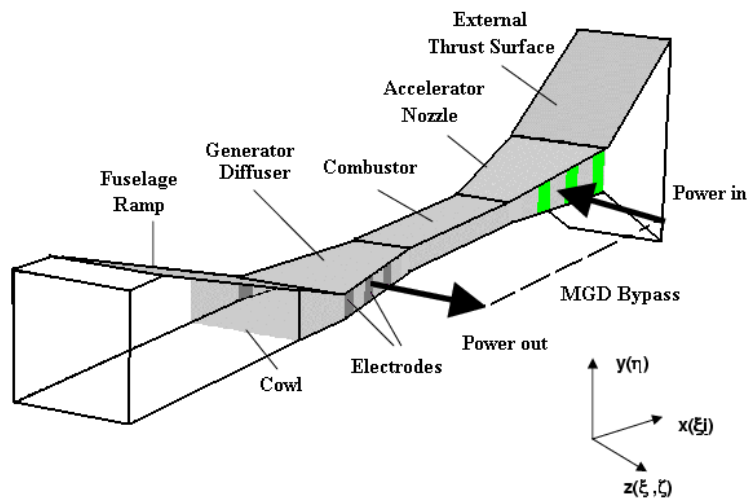


Figure 1.5 Simplified Mach 8 scramjet model design[10]

3 contains a description of the computation setup as well as the specific thrust and efficiency models that were employed. The results follow in Chapter 4 which presents overall specific thrust, quasi one dimensional interpretations of specific thrust, and three dimensional flow field plots. Chapter 4 ends with a discussion of the efficiency of MGD acceleration. Chapter 5 concludes with remarks on what was discovered from the research and what may be considered for future research.

2. Governing Equations

2.1 Navier-Stokes Equations

The Navier-Stokes equations (NSE) govern the behavior of fluid motion. They represent conservation of mass, momentum, and energy. When radiative heat transfer and body forces are neglected, these laws are expressed in the following differential equations[7]:

$$\frac{\partial \rho}{\partial t} + \frac{\partial(\rho V_i)}{\partial x_i} = 0 \quad (2.1)$$

$$\frac{\partial(\rho V_i)}{\partial t} + \frac{\partial(\rho V_i V_j)}{\partial x_j} = -\frac{\partial p}{\partial x_i} + \frac{\partial \tau_{ij}}{\partial x_j} \quad (2.2)$$

$$\frac{\partial(\rho e_t)}{\partial t} + \frac{\partial(\rho h_t V_j)}{\partial x_j} = \frac{\partial(-q_j + \tau_{ji} V_i)}{\partial x_j} \quad (2.3)$$

where i and j refer to directions x and y .

Eqns. 2.2 and Eqn. 2.3 contain the stress tensor, τ_{ij} , and the heat flux vector, q_j , which are defined below,

$$\tau_{ij} = \mu_f \left(\frac{\partial V_i}{\partial x_j} + \frac{\partial V_j}{\partial x_i} \right) - \frac{2}{3} \delta_{ij} \mu_f \frac{\partial V_k}{\partial x_k} \quad (2.4)$$

$$q_j = -\kappa_f \frac{\partial T}{\partial x_j} \quad (2.5)$$

The equations above incorporate molecular viscosity, μ_f , and thermal conductivity, κ_f , which are found using Sutherland's Law and the local temperature, T . These equations are listed below,

$$\mu_f \approx \mu_{0,f} \left(\frac{T}{T_0} \right)^{\frac{3}{2}} \frac{T_0 + S_{\mu_f}}{T + S_{\mu_f}} \quad (2.6)$$

$$\kappa_f \approx \kappa_{0,f} \left(\frac{T}{T_0} \right)^{\frac{3}{2}} \frac{T_0 + S_{\kappa_f}}{T + S_{\kappa_f}} \quad (2.7)$$

where $\mu_{0,f} = 1.716 \times 10^{-5}$, $T_0 = 273$ K, $S_{\mu_f} = 111$ K, $\kappa_{0,f} = 2.41 \times 10^{-2}$, and $S_{\kappa_f} = 194$ K for air[7].

2.1.1 Ideal Gas Law. The NSE above have five equations and six unknowns, (ρ, u, v, w, p, e_t) . In order to complete the computations, the ideal gas law is used[7]. The ideal gas law assumes that air is a calorically perfect gas so the pressure is directly proportional to density, ρ , and temperature, T ,

$$p = \rho \mathcal{R} T \quad (2.8)$$

where \mathcal{R} is the specific gas constant for air.

Total enthalpy, h_t , and total energy, e_t , result from the ideal gas law. These terms are defined below[7],

$$h_t = h + \frac{1}{2} V_i V_i \quad (2.9)$$

$$e_t = h_t - \frac{p}{\rho} \quad (2.10)$$

2.1.2 Vector Form of the Navier-Stokes Equations. The conservative vector form of the NSE is shown below,

$$\frac{\partial \mathbf{U}}{\partial t} + \frac{\partial \mathbf{E}}{\partial x} + \frac{\partial \mathbf{F}}{\partial y} + \frac{\partial \mathbf{G}}{\partial z} = S \quad (2.11)$$

\mathbf{U} is called the vector of conservative variables, given by the following:

$$\mathbf{U} = [\rho \quad \rho \mathbf{u} \quad \rho v \quad \rho w \quad \rho e_t]^T \quad (2.12)$$

\mathbf{E} , \mathbf{F} , and \mathbf{G} are the total fluxes in the corresponding x, y, and z-directions. These are each separated into an inviscid flux vector minus a viscous flux vector[7]:

$$\mathbf{E} = E_i - E_v = \begin{bmatrix} \rho u \\ \rho u^2 + p \\ \rho uv \\ \rho uw \\ \rho h_t u \end{bmatrix} - \begin{bmatrix} 0 \\ \tau_{xx} \\ \tau_{xy} \\ \tau_{xz} \\ u\tau_{xx} + v\tau_{xy} + w\tau_{xz} + q_x \end{bmatrix} \quad (2.13)$$

$$\mathbf{F} = F_i - F_v = \begin{bmatrix} \rho v \\ \rho uv \\ \rho v^2 + p \\ \rho vw \\ \rho h_t v \end{bmatrix} - \begin{bmatrix} 0 \\ \tau_{xy} \\ \tau_{yy} \\ \tau_{yz} \\ u\tau_{xy} + v\tau_{yy} + w\tau_{yz} + q_y \end{bmatrix} \quad (2.14)$$

$$\mathbf{G} = G_i - G_v = \begin{bmatrix} \rho w \\ \rho uw \\ \rho vw \\ \rho w^2 + p \\ \rho h_t w \end{bmatrix} - \begin{bmatrix} 0 \\ \tau_{xz} \\ \tau_{yz} \\ \tau_{zz} \\ u\tau_{xz} + v\tau_{yz} + w\tau_{zz} + q_z \end{bmatrix} \quad (2.15)$$

For non-MGD cases, the source term, \mathbf{S} , is equal to the zero vector,

$$\mathbf{S} = \begin{bmatrix} 0 \\ 0 \\ 0 \\ 0 \\ 0 \end{bmatrix} \quad (2.16)$$

2.2 *Special Relativity*

Since MGD utilizes electromagnetic fields, which essentially consist of light waves, special relativity was considered in the development of the MGD equations. However, the special relativity terms were determined to be negligible and were not implemented in the code.

2.2.1 Reference Frames. There are two reference frames associated with MGD equations. One refers to the coordinate system of the observer who may be in the cockpit of a scramjet driven aircraft or a scientist in the lab. This frame is called the lab frame because its usually associated with the inertial reference frame of a lab. The other frame refers to the coordinate system of the moving fluid. This frame is called the rest frame because it is associated with the coordinate system that is resting on a particle that is moving with the fluid[18].

2.2.2 Lorentz Transformations. The Lorentz transformations (LT) consist of the following equations that transform from the lab frame to the rest frame,

$$x' = \beta(x - Vt) \tag{2.17}$$

$$t' = \beta\left(t - \frac{Vx}{c^2}\right) \tag{2.18}$$

where the primes refer to the rest frame; V is velocity magnitude of flow and c is the speed of light. In the above equations, β accounts for coordinate system warping due to special relativity effects and is defined below:

$$\beta = \frac{1}{\sqrt{1 - \frac{V^2}{c^2}}} \tag{2.19}$$

In order to transform from a vector in one reference frame to a vector in another reference frame moving at a substantially fast velocity the Silberstein operator α , also known as the stretching operator[18], is used.

$$\alpha \vec{G} = \vec{G} + \frac{(\beta - 1)\vec{V}(\vec{V} \cdot \vec{G})}{\|\vec{V}\|^2} \quad (2.20)$$

This operator utilizes the β term and the velocity of the rest frame with respect to the lab frame. The vector \vec{G} is arbitrary. For this study, \vec{G} could be the Lorentz force, electric field, or the current density.

2.3 Maxwell Equations

The Maxwell equations (ME) are the governing equations for electromagnetics. They are valid in both the lab frame and the reference frame[7].

$$\nabla \cdot \vec{D} = \rho_e \quad (2.21)$$

$$\nabla \cdot \vec{B} = 0 \quad (2.22)$$

$$\nabla \times \vec{E} = -\frac{\partial \vec{B}}{\partial t} \quad (2.23)$$

$$\nabla \times \vec{H} = \vec{j} + \frac{\partial \vec{D}}{\partial t} \quad (2.24)$$

where \vec{D} is the electric flux density, \vec{B} is the magnetic flux density, \vec{E} is the electric field, \vec{H} is the magnetic field, \vec{j} is the conduction current density, and ρ_e is the space charge.

The ME consist of four equations and seven unknowns. Three more relations are used to balance the system. One of which is Ohm's Law, and the remaining two are the constitutive relations[18].

2.3.1 Ohm's Law. Ohm's law is defined in terms of anisotropic media, which means that the conductivity, σ , depends on the orientation of the particle. The anisotropic quality is expressed with the directional subscripts i and j . The expression is simple in the rest frame,

$$j'_i = \sigma_{ji} E'_j \quad (2.25)$$

However, Ohm's law does not transform into the lab frame as easily as the ME. Instead, Ohm's law depends on the Maxwell-Lorentz transformations (MLT). The MLT are derived after several substitutions and partial differentiations of the ME and LT, Ohm's law, and the constitutive relations[18]. Briefly, Ohm's law becomes,

$$j_i = \left(\frac{\beta}{\alpha}\right)\{\sigma_{ji}[E_j + (\vec{V} \times \vec{B})_j]\} + \rho_e V_i \quad (2.26)$$

since $V^2 \ll c^2$ for flow velocities around Mach 8, the $(\frac{\beta}{\alpha})$ term equals one. Ohm's law then becomes,

$$j_i = \sigma_{ji}[E_j + (\vec{V} \times \vec{B})_j] + \rho_e V_i \quad (2.27)$$

2.3.2 Constitutive Relations. The two constitutive relations for linear isotropic dielectrics and magnetic materials expressed in the rest frame are listed below,[18]:

$$\vec{E}' = \frac{\vec{D}'}{\epsilon_e} \quad (2.28)$$

$$\vec{B}' = \mu_e \vec{H}' \quad (2.29)$$

where subscript 0 represents the freespace value.

With application of MLT, the above constitutive relations can be transformed to the lab frame. When $V^2 \ll c^2$ and the fluid is isotropic, the constitutive relations become[18],

$$\vec{D} = \epsilon_e[\vec{E} + (1 - \frac{1}{\frac{\epsilon_e}{\epsilon_{0,e}} \frac{\mu_e}{\mu_{0,e}}})\vec{V} \times \vec{B}] \quad (2.30)$$

$$\vec{B} = \mu_e \left[\vec{H} - \left(1 - \frac{1}{\frac{\epsilon_e}{\epsilon_{0,e}} \frac{\mu_e}{\mu_{0,e}}} \right) \vec{V} \times \vec{D} \right] \quad (2.31)$$

2.3.3 Magnetogasdynamic Assumptions. A current moving through a stationary object in an electric field produces a Lorentz force in a direction perpendicular to the field and the direction of current flow. In fluids, a force acting on the flow is called a body force. The Lorentz body force density for anisotropic moving media in the rest frame is defined below[18],

$$\vec{f}_e = \rho_e \vec{E} + \vec{j} \times \vec{B} - \frac{\epsilon_0}{2} E^2 \nabla \kappa - \frac{\mu_0}{2} H^2 \nabla \kappa_m + \frac{\epsilon_0}{2} \nabla \left(E^2 \frac{\partial \kappa}{\partial \rho} \right) + \frac{\mu_0}{2} \nabla \left(H^2 \frac{\partial \kappa}{\partial \rho} \right) \quad (2.32)$$

where the subscript m represents the magnetostriction term.

The above equation is complex, and is only valid in the rest frame. However, the body forces can be simplified, for the lab frame, given the following six assumptions[10]:

MGD Assumption 1: $|V|^2 \ll c^2$. The magnitude of the velocities in MGD are much less than the speed of light so β approaches one.

MGD Assumption 2: $\vec{E} \approx \mathcal{O}(\vec{V} \times \vec{B})$. The applied magnetic field is much greater than the induced magnetic field.

MGD Assumption 3: $\frac{\partial \vec{D}}{\partial t} \approx 0$, so $\frac{\partial \vec{E}}{\partial t} \approx 0$, and $\nabla \times \vec{B} = \mu_e \vec{j}$. The electric field has no high frequencies.

MGD Assumption 4: $\epsilon \vec{E}^2 \ll \frac{\vec{B}^2}{\mu_e}$. Magnetic energy is orders of magnitude greater than the electric energy.

MGD Assumption 5: $\vec{j} = \sigma(\vec{E} + \vec{V} \times \vec{B})$. The conductivity is independent of electric field, and constant with frequency. This means that $\vec{j}' = \vec{j}$.

MGD Assumption 6: $\vec{f} = \rho_e \vec{E} + \vec{j} \times \vec{B}$. The body force density is homogenous and independent of electrostriction and magnetostriction. Since $\rho_e \vec{E} \ll \vec{j} \times \vec{B}$, then $\vec{f} = \vec{j} \times \vec{B}$ is used.

2.3.4 Maxwell's Equations for Magnetogasdynamic Flow. The six assumptions listed above can be applied to the original ME. In the lab frame they are the following[18]:

$$\nabla \times \vec{E} = -\frac{\partial \vec{B}}{\partial t} \quad (2.33)$$

$$\nabla \times \vec{B} = \mu_e \vec{j} \quad (2.34)$$

$$\nabla \cdot \vec{j} = 0 \quad (2.35)$$

$$\nabla \cdot \vec{B} = 0 \quad (2.36)$$

Ohm's law is,

$$\vec{j} = \sigma(\vec{E} + \vec{V} \times \vec{B}) \quad (2.37)$$

All subsequent equations are written in the lab frame.

2.4 Magnetogasdynamic Equations

The magnetogasdynamic equations incorporate ME and the NSE for MGD. These equations describe the interaction between electromagnetic fields and electrically conducting gases in a continuum governed by the MGD assumptions. The magnetogasdynamic equations are the same as those given in Eqns. 2.11 except the term \mathbf{S} is now given by:

$$\mathbf{S} = \begin{bmatrix} 0 \\ j_y B_z - j_z B_y \\ j_z B_x - j_x B_z \\ j_x B_y - j_y B_x \\ E_x j_x + E_y j_y + E_z j_z \end{bmatrix} \quad (2.38)$$

The three middle rows refer to the three components of the $(\vec{j} \times \vec{B})$ Lorentz force. The last row, equivalent to $\vec{E} \cdot \vec{j}$, is the resulting energy interaction which accounts for Joule heating and the work of the Lorentz body force.

2.4.1 Non-dimensionalizing the Magnetogasdynamic Equations. In order to avoid machine limitations in the computational code, the MGD equations are non-dimensionalized. In the following relations, dimensionless quantities are flagged with an asterisk[7]:

$$\begin{aligned} L^* &= \frac{L}{L_0} & \vec{V}^* &= \frac{\vec{V}}{V_0} \\ \rho^* &= \frac{\rho}{\rho_0} & T^* &= \frac{T}{T_0} \\ \vec{E}^* &= \frac{\vec{E}}{E_0} & \vec{B}^* &= \frac{\vec{B}}{B_0} \end{aligned} \quad (2.39)$$

These initial dimensional freestream quantities with the subscript 0 are used to non-dimensionalize the other variables, and all dimensionless variables are substituted into the equations. Several non-dimensional parameters are formed during this process which help to characterize MGD flows. The Reynolds number is the ratio of inertial forces to viscous forces,

$$Re = \frac{V_0 L_0}{\nu_f} \quad (2.40)$$

where.

$$\nu_f = \frac{\mu_f}{\rho} \quad (2.41)$$

The magnetic Reynolds number is a measure of the magnitude of the induced magnetic field compared to the total magnetic field:

$$Rm = V_0 L_0 \sigma_0 \mu_{0,e} \quad (2.42)$$

The Mach number and magnetic Mach number are listed below,

$$M = \frac{V_0}{a_0} \quad (2.43)$$

$$M_m = \frac{V_0 \sqrt{\rho_0 \mu_{0,e}}}{B_0} \quad (2.44)$$

The Prandtl number is the ratio of kinematic viscosity to thermal diffusivity[7]:

$$Pr = \frac{c_P \nu_f \rho_0}{\kappa_f} \quad (2.45)$$

The magnetic Prandtl number is the ratio of viscous diffusion to magnetic diffusion:

$$Pm = \sigma_0 \nu_f \mu_{0,e} = \frac{Rm}{Re} \quad (2.46)$$

The interaction parameter, \mathcal{Q} , is used when $Rm \ll 1$. \mathcal{Q} is the ratio of the ponderomotive force to the inertial force, which should be about one. An increase in \mathcal{Q} causes an increase in the strength of the magnetic field.

$$\mathcal{Q} = \frac{\sigma_0 B_0^2 L_0}{\rho_0 V_0} = \frac{Rm}{M_m^2} \quad (2.47)$$

The ratio of the electric field to the induced effects is known as the load factor, \mathcal{K} ,

$$\mathcal{K} = \frac{-E_0}{B_0 V_0} \quad (2.48)$$

where \mathcal{K} is proportional to the applied electric field, E_0 , and voltage differential, $\Delta\phi$.

In the non-dimensional MGD equations, the non-dimensional Lorentz force is $\mathcal{Q}(\vec{j}^* \times \vec{B}^*)$ and the non-dimensional energy interaction is $\mathcal{Q}(\vec{E}^* \cdot \vec{j}^*)$.

3. Computational Set-Up

3.1 MGD 3-D Computational Code

The computational study employed a 3-D non-dimensional CFD code. The code was written by AFRL/VAAC[10, 11, 12, 13, 14, 15, 27, 29]. The code solves the Euler and Navier Stokes equations with the source term for MGD Lorentz Forces and Energy Interaction.

In the Hypersonic case, high speed fluids involve discontinuities in the flow solution. In order to capture these discontinuities, flux vectors are calculated using Roe's flux difference splitting scheme with van Leer harmonic limited Monotone upstream-centered schemes for conservation laws (MUSCL)[11, 12, 13, 14, 28, 29] which provide up to third-order spatial accuracy. Since the Roe scheme is capable of producing non-physical expansion shocks under certain constraints, an entropy fix was added to negate this effect.

3.2 Thrust Calculation Model

It is common to evaluate the stream thrust function at the inlet and outlet of a nozzle to determine the thrust provided by the nozzle. The equation for specific thrust is defined in terms of the stream thrust function,

$$\frac{F}{\dot{m}} = Sa_{exit} - Sa_{inlet} \quad (3.1)$$

However, a better measure of the effect each segment of electrode and insulated region has on the thrust was found by plotting out the stream thrust function over the entire length of the nozzle. This way stream thrust could be interpreted based on the location within the stream.

The stream thrust function is defined [17] as,

$$Sa = \frac{I}{\dot{m}} \quad (3.2)$$

where the axial force function, I , is,

$$I = pA(1 + \gamma M^2) \quad (3.3)$$

I measures the axial force between two stations. The above equation is based on the following assumptions[16].

Sa Assumption 1: The flow is steady or quasi steady.

Sa Assumption 2: The ratio of momentum flux to pressure forces is large.

Sa Assumption 3: Thermochemistry of the flow must be known.

Sa Assumption 4: The velocity component at each stage aligned with the thrust or axial direction and perpendicular to the through-flow area is used to calculate the Mach number.

Steady flow inertial terms are large in hypersonic flow, so Assumption 1 is valid. Assumption 3 assumes that thermochemistry was known. This can be assumed since the atmosphere is primarily composed of N_2 and O_2 molecules which do not significantly ionize at Mach numbers less than 9[31].

The stream thrust function can then be simplified for axial thrust in the following equation:

$$Sa_i = u_i(1 + \frac{\mathcal{R}T_i}{u_i^2}) \quad (3.4)$$

The value of Sa_i , where i represents a given index along the x-axis, was then plotted for all values of x . The difference between the exit and inlet conditions served as a measure of total stream thrust produced in the nozzle.

3.3 Efficiency Computation Model

For this study, the efficiency of MGD acceleration was described by the following relationship,

$$\eta \equiv \frac{\Delta P_{out}}{\Delta P_{in}} \quad (3.5)$$

ΔP_{out} , is the increase in power due to the MGD accelerator. This can be determined by subtracting a baseline (no-MGD) power output from any investigated MGD case. The power output due to the MGD accelerator can be expressed in terms of the increase in the product of thrust and velocity[17]. The velocity for this study will be taken as the change in velocity between the inlet and exit of the nozzle, Δu .

$$\Delta P_{out} = [(\frac{F}{\dot{m}})\dot{m}\Delta u]_{MGD} - [(\frac{F}{\dot{m}})\dot{m}\Delta u]_{Baseline} \quad (3.6)$$

where \dot{m} is the mass flow rate which is defined as $\rho u A$ in which A is the area of the cross section of the nozzle. Since \dot{m} remains constant by definition, it did not matter where it was calculated. For consistency, it was calculated at the exit plane.

Assuming that the magnetic field originates from a permanent magnet, which is not augmented with any electromagnetic fields, power input, ΔP_{in} , is actually the sum of the power requirements of the two major components that make MGD acceleration possible. These included the power requirement that maintained the electric potential, $\Delta P_{in\Delta\phi}$, and that which maintained the conductivity pattern, $\Delta P_{in\sigma}$.

$$\Delta P_{in} = \sum \Delta P_{in\Delta\phi_n} + \Delta P_{in\sigma} \quad (3.7)$$

where n is the index for the electrode. In this study, there were only three electrodes so n ranged from 1 to 3.

The value of $\Delta P_{in\sigma}$ could be found using a separate solver for ionization based on flow parameters[21]. However, This study does not attempt to calculate the power requirements due to the conductivity pattern. It should just be noted that the efficiency values obtained are inflated due to the omission of this term. In subsequent chapters, this inflated efficiency will be referred to as pseudo efficiency.

The power requirements for the electric potential, $\Delta\phi$, whose SI units are Volts[6], were determined from basic principles in electricity[30]. Figure 3.1 is a diagram of the electrodes. Each set of electrodes consisted of an anode and a cathode based on electric potential, ϕ . The space between was a medium of air with its own conductivity value, σ . The distance between the electrodes was ℓ .

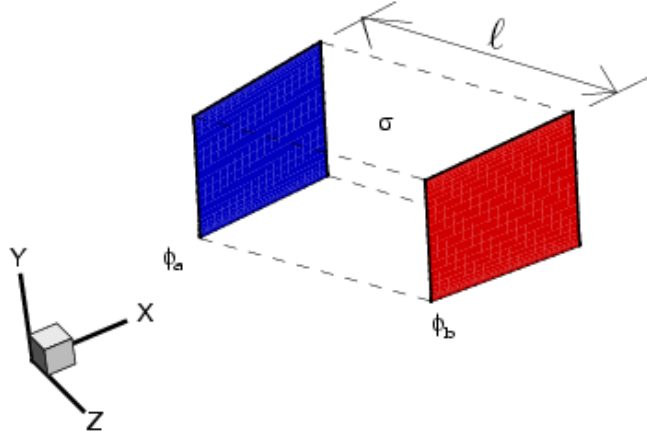


Figure 3.1 Diagram of electrodes.

For simplicity, \vec{E} was assumed to be constant in the z-direction,

$$\Delta\phi = \phi_b - \phi_a = - \int_a^b \vec{E} \cdot d\vec{s} = E \int_0^\ell dx = E\ell \quad (3.8)$$

Given the above equation, Eqn. 3.8, and Ohm's law, as defined in the rest frame from Eqn. 2.27, Ohm's law can be rewritten in terms of the width of the nozzle between the electrodes, ℓ , and the electric potential, $\Delta\phi$ in Eqn. 3.9.

$$j = \sigma \left[\frac{\Delta\phi}{\ell} - UB \right] \quad (3.9)$$

Here, the $-UB$ term results from the property that $\vec{U} \times \vec{B}$ is working against the electric potential. For reference, charge flux, j , is defined as,

$$j \equiv \frac{I}{A} \quad (3.10)$$

where I is equal to current and A is the cross sectional area of the electrode. Assuming \vec{E} is in the z-direction, the terms in Eqn. 3.9 are rearranged to solve for I in Eqn. 3.11.

$$I = \sigma A \left[\frac{(\Delta\phi)}{\ell} - UB \right] \quad (3.11)$$

Since electric power is defined as,

$$P \equiv \Delta\phi I \quad (3.12)$$

Eqn. 3.11 and Eqn. 3.12 can be used to determine the power input requirements due to the electric potential.

$$\Delta P_{in_{\Delta\phi}} = \sigma A \left[\frac{(\Delta\phi)^2}{\ell} - UB(\Delta\phi) \right] \quad (3.13)$$

Eqn. 3.13 was then used to determine the value of $P_{in_{\Delta\phi}}$ in Eqn. 3.7.

3.4 Computational Domain

The computational domain for the MGD accelerator was derived from an AJAX type MGD scramjet engine investigated by Gaitonde [10]. The dimensions of the MGD accelerator portion of the nozzle appear in Figure 3.2. The measurements were provided by Harrington[16]. The inlet area is 0.1075 m² and the exit area is 0.4335 m². This difference was on account of a 4° divergence in the top and each side wall. The exit to inlet area ratio was 4.032.

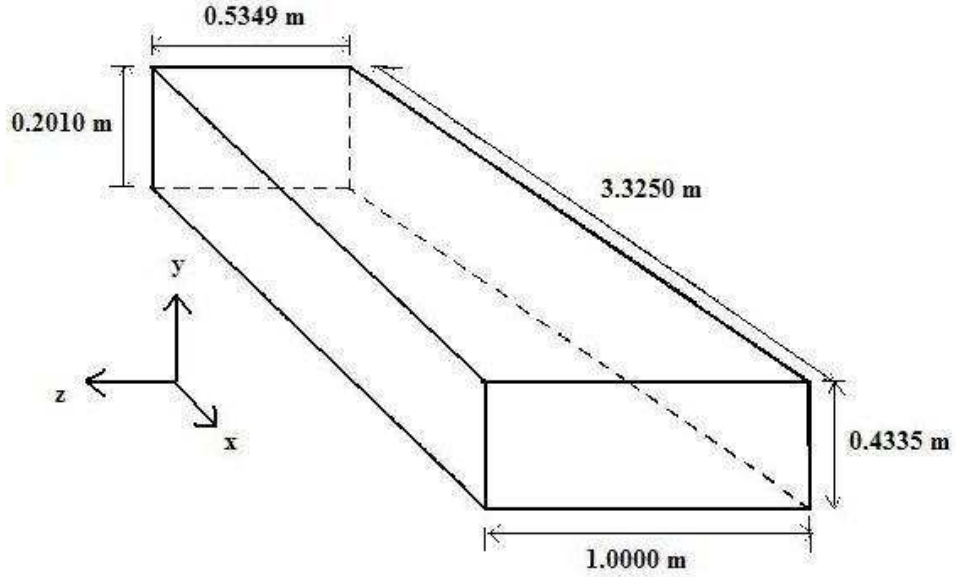


Figure 3.2 Three dimensional MGD accelerator geometry.

The grid used for the computations was built from Harrington's [16] domain in which Gridgen v15 was used to develop a laminar grid. This laminar grid has ten cells in the boundary layer. The boundary layer thickness, determined using laminar boundary layer theory, was 5.38 mm. The orthogonal grid solver was used to mesh the outer grid lines perpendicular to the walls. The index dimensions of the grid were 120 x 46 x 56 nodes which provided 297,000 cells[16].

3.5 Computational Parameters

The flow conditions used at the accelerator inlet were set using the Mach 8 design flight conditions which were employed by Harrington[10]. Table 3.1 lists the free stream conditions and the inlet conditions used in the numerical computations. For reference, Table 3.1 also lists the non-dimensional values of the inlet conditions when ratio of specific heat is set to 1.23.[16]

Throughout the results, dimensional values are computed from non-dimensional data using the equations listed in Table 3.2. These values are the fixed parameters in the scientific method.

Table 3.1 Freestream and MGD Accelerator Inlet Conditions.

	Free-stream Conditions	Inlet Conditions	Non-Dimensional Inlet Conditions
Velocity	2380.45 m/s	1938.2 m/s	0.8142
Temperature	250 K	2892.0 K	11.568
Pressure	1285.76 Pa	143116 Pa	1.4101
Mach	8	1.9148	1.9148

Table 3.2 Dimensional Conversion Factors.

	Symbol	Multiply by Expression	Multiply by Value	Units
Position	X	L_0	0.6	m
	Y			
	Z			
Velocity	U	U_0	2380.45	$\frac{m}{s}$
	V			
	W			
Pressure	P	P_0	1285.76	Pa
Density	ρ	$\frac{P_0}{287.0 \cdot T_0} = \rho_0$	0.01792	$\frac{kg}{m^3}$
Temperature	T	T_0	250	K
Magnetic Flux Density	B_y	B_0	10	T
Electric Potential	ϕ	$U_0 L_0 B_0 = \phi_0$	14282.7	$Volts$
Conductivity	σ	$\frac{\rho_0 \cdot U_0}{B_0^2 \cdot L_0} = \sigma_0$	0.710961	mho/m

This study investigates the effect of two independent parameters. The first of which is the conductivity pattern. There were two assumed conductivity patterns which were designed to simulate electron beam ionization. In both patterns, the non-dimensional σ^* is set to unity in the center of the accelerator and it decreases in a modified Gaussian distribution to a given value at the walls[13]. Conductivity pattern 2 has a larger area of high conductivity in the axial direction.

Figure 3.3 and Figure 3.4 show the conductivity patterns on two cut planes in the accelerator nozzle to illustrate the three dimensional nature of the conductivity. Conductivity pattern 1 shown in Figure 3.3 has a smaller range in the x-direction than conductivity pattern 2 in Figure 3.4. Both conductivity patterns assume that $\sigma_0 = 0.710961 \frac{mho}{m}$. A $Z = 0$ m slice, and a $Y = 0.15$ m slice were chosen to convey the pattern along the axial coordinates of accelerator.

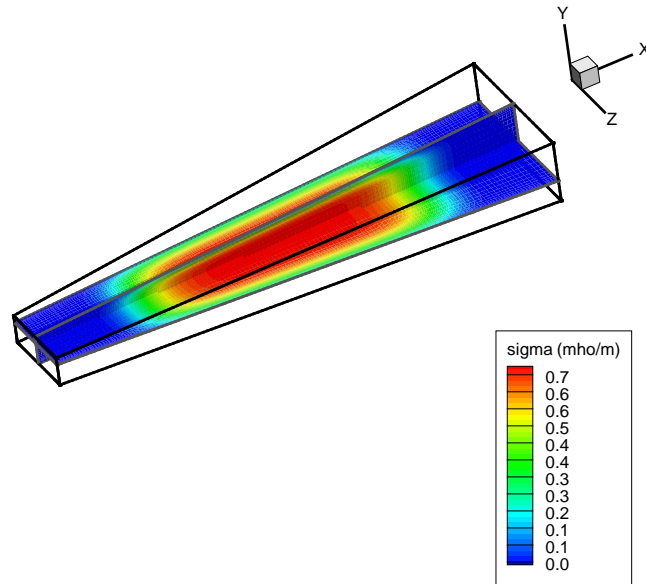


Figure 3.3 Three dimensional conductivity pattern 1.

The dimensional values of σ are used to determine the magnetic flux density, B_0 , which may vary nominally from 2 Tesla to 10 Tesla[16]. By setting the interaction parameter, \mathcal{Q} , to unity and rearranging the terms Eqn. 2.47 becomes:

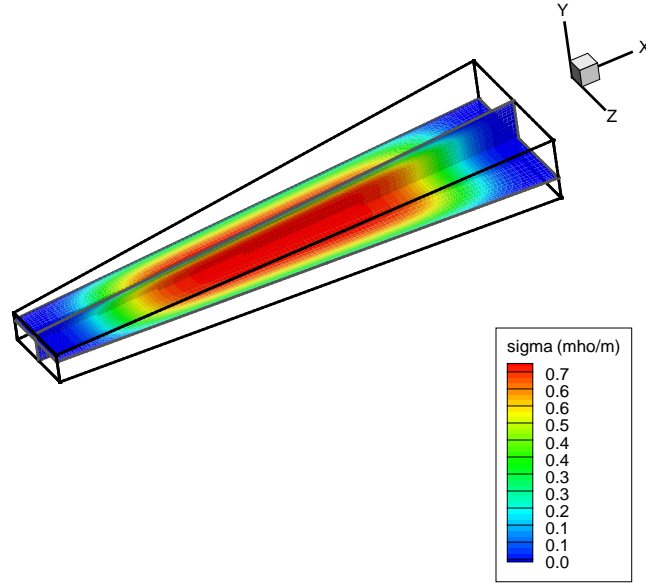


Figure 3.4 Three dimensional conductivity pattern 2.

$$B_0 = \sqrt{\frac{\rho_0 U_0}{\sigma_0 L_0}} \quad (3.14)$$

in which L_0 is 0.6, and ρ_0 and V_0 are the free-stream values from Table 3.2. This means that the values of σ_0 and B_0 depend on one another such that if a σ_0 of $0.710961 \frac{mho}{m}$ is chosen then the accelerator requires a magnetic flux density of 10 T; or if a σ_0 of $17.778 \frac{mho}{m}$ is chosen then 2 T[16]. For our study, B_0 was assumed to be 10 T.

The second independent parameter in this study was the load factor, \mathcal{K} , which was given in Eqn. 4.1. The magnetic flux density is non-dimensionalized to unity. This means that changes in the load factor cause changes in E_0 , the magnitude of the applied electric field. Thus the load factor becomes a measure of the applied electric field intensity[16].

The Lorentz force given as $\vec{j} \times \vec{B}$ is applied to accelerate the flow in the MGD solution runs. The magnetic flux density, B , is oriented in the positive y direction. For the load factors greater than 1.0, an electric current is produced in the negative

z direction which results in an accelerating Lorentz force in the positive x direction. For the load factors less than 1.0, the induced effects are greater than the electric field so electric energy is generated causing decelerated flow in the x direction.

3.6 Computational Cases

The flow solution was allowed to converge without any MGD interaction. This case was called the Baseline, and its converged solution was used as the initial conditions for all of the subsequent cases[16].

The subsequent cases involved MGD interaction. MGD acceleration is defined by a load factor, \mathcal{K} , greater than 1.0 and generation is defined by a load factor less than 1.0. The independent parameters of conductivity pattern was also varied.

The generating load factors investigated were 0.8 and 0.9 for both sigma patterns. The accelerating load factors ranged from 1.2 to 1.6. Table 3.3 shows the naming convention used in Chapters 4 and 5 for the investigated cases.

Table 3.3 Naming Scheme for Investigated Cases.

Load Factor (\mathcal{K})	Conductivity σ -pattern 1	Conductivity σ -pattern 2
0.8	K08	K08_SIG2
0.9	K09	K09_SIG2
1.2	K12	K12_SIG2
1.4	K14	K14_SIG2
1.6	K16	K16_SIG2

The K10 case still has a voltage potential across the electrodes except the electric field, E , is set equal to the UB term. K10 is thus different from the baseline case which does not include electrodes at all.

The voltage potential for each electrode, $\Delta\phi$ was determined using the following equation:

$$\Delta\phi = \mathcal{K}\ell U_{ref} B \tag{3.15}$$

where ℓ is the width between the two electrodes.

4. Results

The MGD accelerator described in Chapter 3 was used in this numerical study to investigate the influence of accelerating and decelerating load factors. Table 3.3 shows the nomenclature used for the different runs. The Non-MGD baseline case was run to convergence and then used as a reference in later MGD solutions. The objective was to determine performance outcome based on the specific thrust and the efficiency of the nozzle. The first section provides the specific thrust and quasi 1-D interpretation of the stream thrust function. This serves as an overview for the following three sections which interpret the behavior of the 3-D flow fields. Then non-MGD baseline, the K16 MGD acceleration, and K08 MGD deceleration cases are investigated in detail to show characteristics of the flow fields. The detail flow field figures of all other MGD cases investigated are presented in Appendix A. Last, the efficiencies of the MGD accelerated cases are presented.

4.1 *Specific Thrust*

Specific thrust for each case was calculated using Eqn. 3.1. The results were arranged in the bar graph shown in Figure 4.1. Cases K12, K14, and K16 increased thrust as expected for both conductivity patterns. These cases accelerated the flow which caused an increase specific thrust over the baseline case. The generators decelerated the flow which caused a decrease in thrust.

In order to interpret the specific thrust results, a quasi 1-D plot of stream thrust, S_a , was investigated over the nozzle length in Figure 4.2 and Figure 4.3 for conductivity patterns 1 and 2. In both of these figures, the K12, K14, and K16 cases showed increase in thrust respectively across each electrode, interspaced with moderate increases in thrust due to the expansion nozzle. In general, the specific thrust in SIG2 was greater than that of SIG1 because the greater conductivity allowed for better current flow.

The behavior of the generator stream thrusts at the first electrode is of interest. Although, the generator cases ultimately decelerated the flow as expected, their

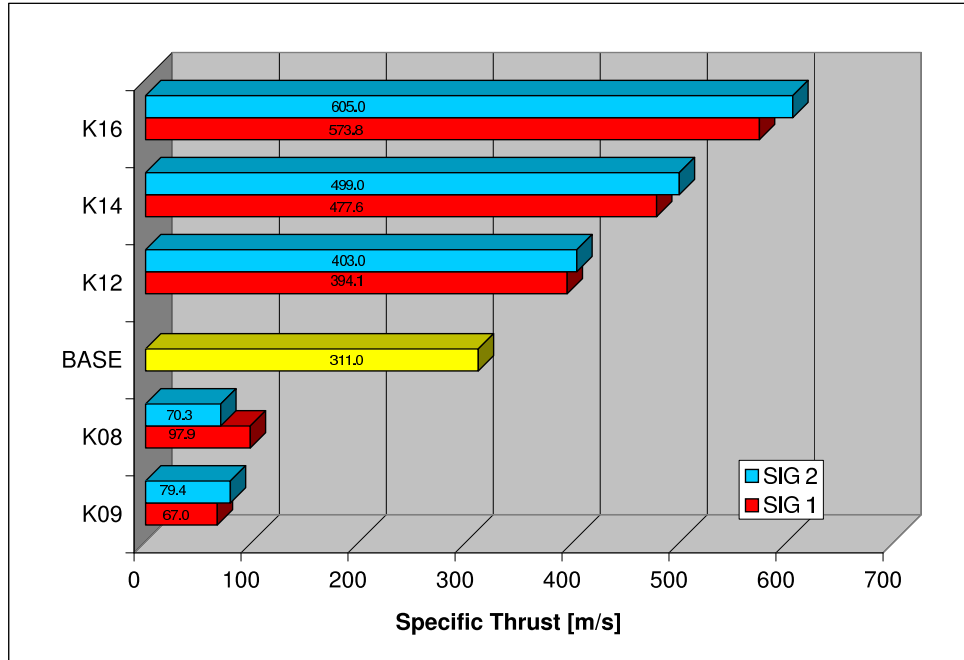


Figure 4.1 Specific Thrusts

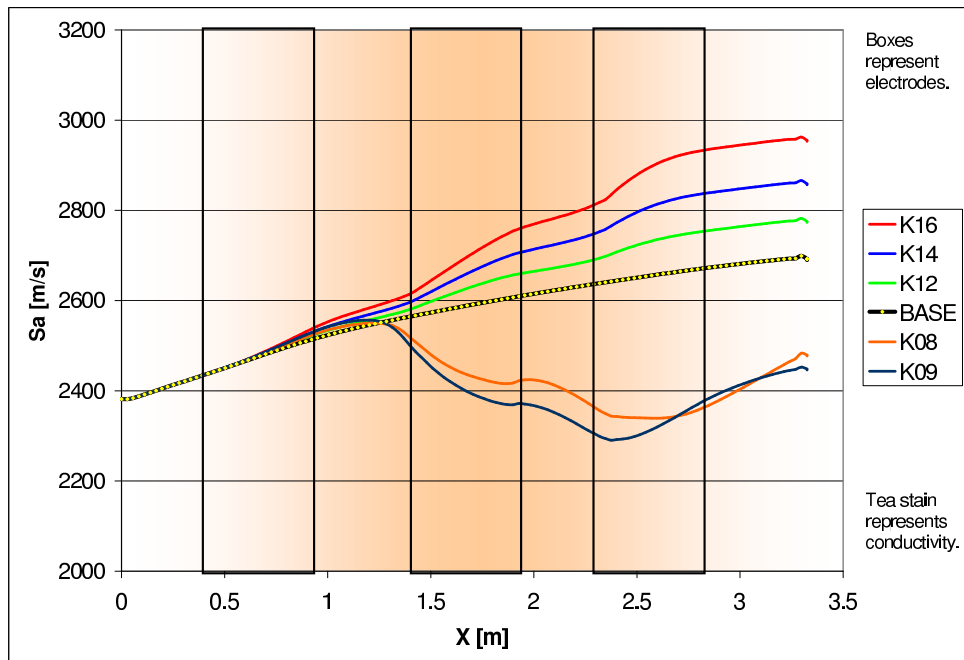


Figure 4.2 Stream Thrust Function for Conductivity 1

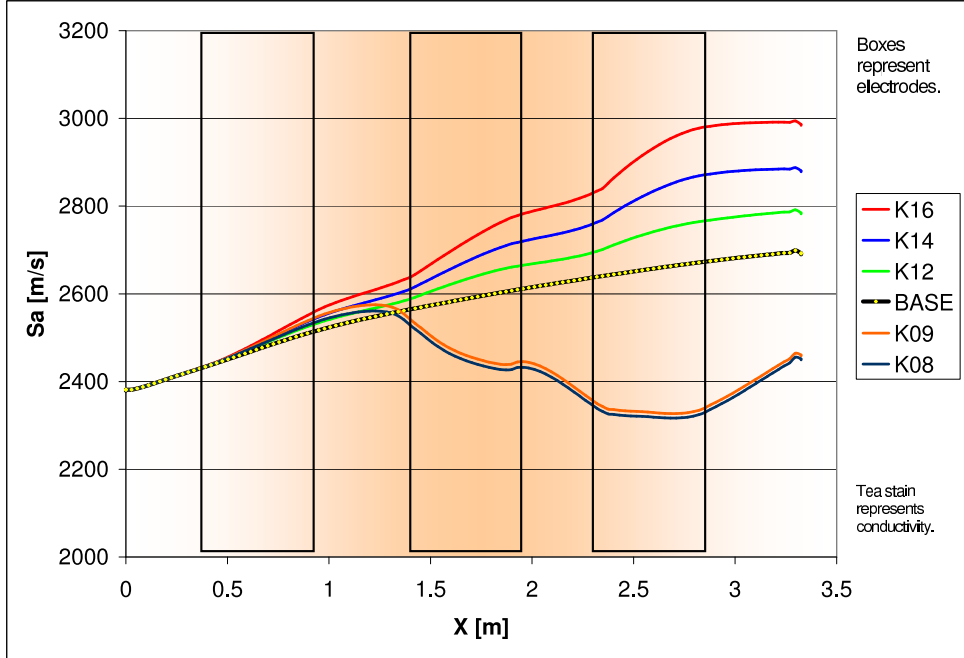


Figure 4.3 Stream Thrust Function for Conductivity 2

stream functions increased at the first electrode. The explanation for this behavior is simple. The load factors were set using the reference velocities of the baseline case. When $\Delta\phi$ in Eqn. 3.15 is fixed, the load factor changes with the local velocity, U_{ref} , as shown in this rearrangement of the equation for voltage potential:

$$\mathcal{K} = \frac{\Delta\phi}{\ell U_{ref} B} \quad (4.1)$$

The field of electric potential is not limited to the region directly between the electrodes. In fact, the leaking field causes the flow to decelerate before reaching the electrode. When the flow has reached the electrode, it has already decelerated slightly from the baseline case. The deceleration continues in a gradual manner, due to the weak ionization at the beginning of the electrode. This sets up the conditions for a change in load factor behavior as the flow decelerates beyond the point at which UB is no longer greater than E (see Eqn. 4.1). The spike in the stream function is

characteristic of the Gaussian distribution for σ , since the electrode becomes more effective as the load factor decreases.

The rest of the generator cases follow a path of acceleration followed by immediate deceleration between the first and second electrodes. This occurred because the potential across the second set of electrodes was set using the local velocity of the baseline case. Since acceleration occurred across the first electrode, the local velocity was greater than expected and ended up artificially decreasing the load factor to that of an MGD generator.

In general, SIG2 had greater specific thrusts for the accelerator and less specific thrusts for the generators when compared to the results for SIG1. The percent increases in specific thrust are shown in Table 4.1 below.

Table 4.1 Percent Difference in Specific Thrust, $\frac{F}{m}$, from baseline case.

Load Factor \mathcal{K}	Conductivity Pattern 1	Conductivity Pattern 2
0.8	-31%	-23%
0.9	-22%	-26%
1.2	27%	30%
1.4	54%	60%
1.6	84%	95%

As expected, thrust decreases for the $\mathcal{K} = 0.8$ and $\mathcal{K} = 0.9$ cases for both conductivity patterns. The magnitude of the percent change is greater for the $\mathcal{K} = 0.8$ case than the $\mathcal{K} = 0.9$ case in the SIG1 pattern. This is expected because there should be more deceleration for the smaller load factors. However, the opposite is true for the SIG2 pattern. It is uncertain what caused this increase in percent difference; so more work needs to be done in the area of the effect of conductivity on MGD generators.

4.2 Baseline Flow field

The baseline solution for the conditions and geometry described in Chapter 3 was computed without MGD interaction. The Mach number in the x-direction of the baseline case is shown in Figure 4.4. Although no load factor is set in the baseline case, the cut planes at $x = 0.72647, 1.67647, 2.62647$ are at the midlines of the electrodes. The flow accelerates from Mach 1.96 at the exit of the combustor to about Mach 3.06 (2480 m/s) at the exit of the nozzle as expected.

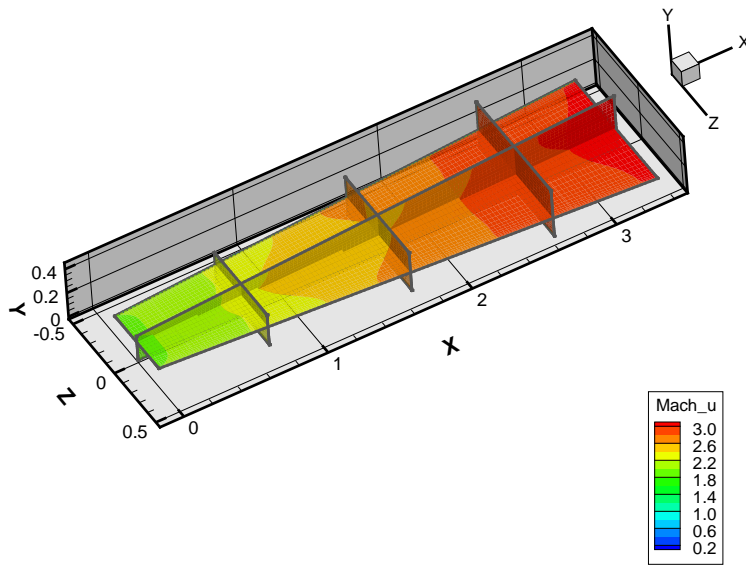


Figure 4.4 Mach Number Contours for Baseline Case

Figure 4.5 shows the baseline temperature contours. The flow temperature decreases as the flow expands, as expected. The temperature of the fluid is 2,658 K in the middle of the inlet plane; and 1,763 K at the exit plane. Higher temperature regions, 3,677 K, are located on the wall surfaces due to stagnation.

Baseline pressure contours are shown in Figure 4.6. The pressure decreases as expected due to geometry expansion in the nozzle. The pressure at the inlet reaches a maximum of 162,537 Pa throughout the entire inlet plane including the walls. The average exit pressure is 21,711 Pa in the exit plane.

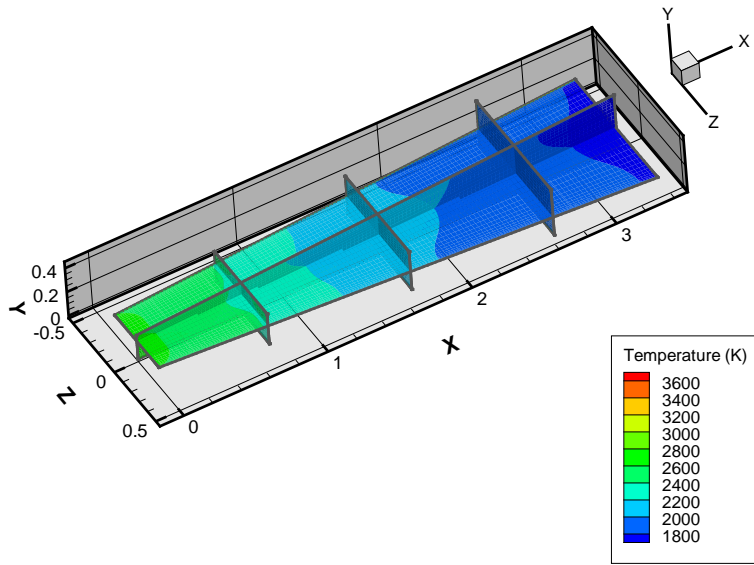


Figure 4.5 Temperature Contours for Baseline Case

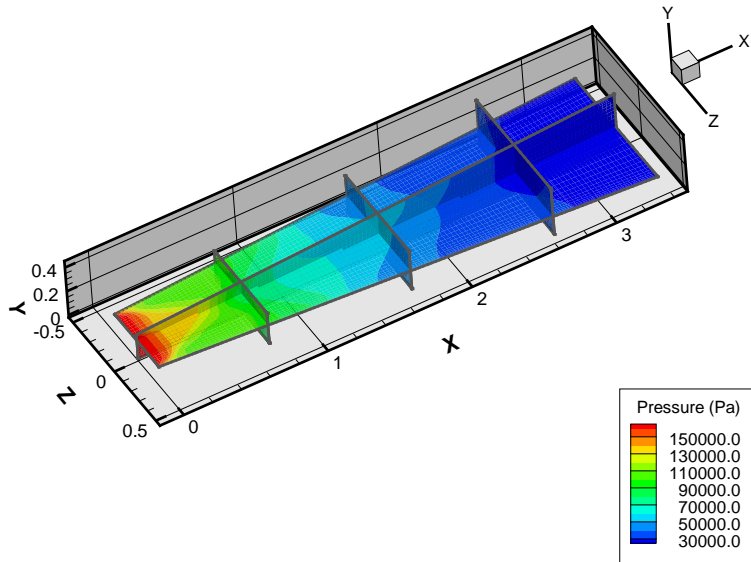


Figure 4.6 Pressure Contours for Baseline Case

4.3 Acceleration Case, $\mathcal{K} = 1.6$

Flow field acceleration occurs when the electric and magnetic fields are oriented such that the resulting Lorentz force accelerates the flow. The K12, K14, K16, SIG2_K12, SIG2_K14, and SIG2_K16 acceleration flow fields were very similar. Therefore, only the K16 case is presented in the results. The flow field plots for the rest of the cases can be found in Appendix A.

The Lorentz force vectors for K16 case on the midplane in the y and z directions are in Figure 4.7. The forces act in an accelerating direction throughout the entire electrode regions as seen in the x-z midplane on top. The vectors accelerate the flow inward toward the center at the leading edge of the electrodes and change their direction along the electrodes to be parallel with the flow. At the end of the electrodes, the vectors push the flow toward the wall. The x-y midplane force vectors show that the largest accelerating forces are at the locations of maximum conductivity, near the center of the nozzle in the x direction.

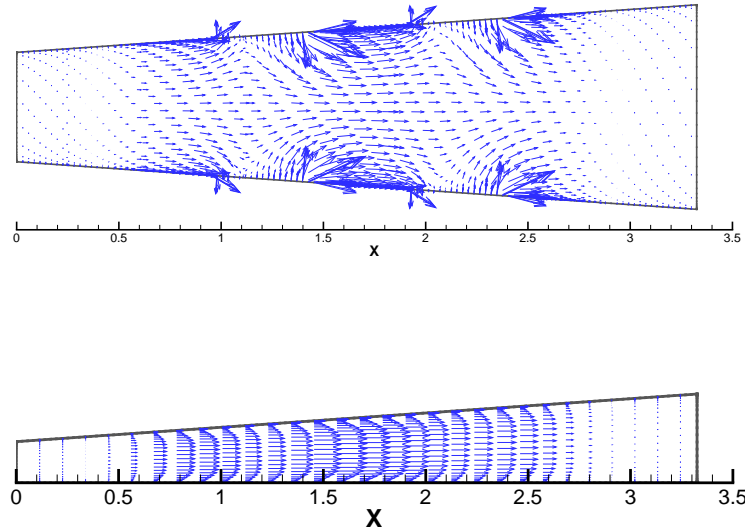


Figure 4.7 K16 Lorentz Force Vectors (top: x-z midplane, bottom: x-y midplane)

The Lorentz force has the effect of increasing the flow velocity and mach number. Figure 4.8 shows how the mach number increases across each electrode. The largest increase in Mach number occurs in the center of the flow field with respect to the x-z plane. This is very similar to the baseline case. However, the accelerated case features long regions of slower Mach number along the walls. This is probably due to a combination of the Lorentz forces pushing against the wall and increases in local temperature along the wall. The maximum Mach number at the exit of the nozzle is 3.13, which is a 2.5% increase over baseline exit Mach number. Negating the effect temperature has on Mach number, the velocity at the exit is 2,730 m/s which is a 10% increase in the exit velocity. The Lorentz force has accelerated the flow.

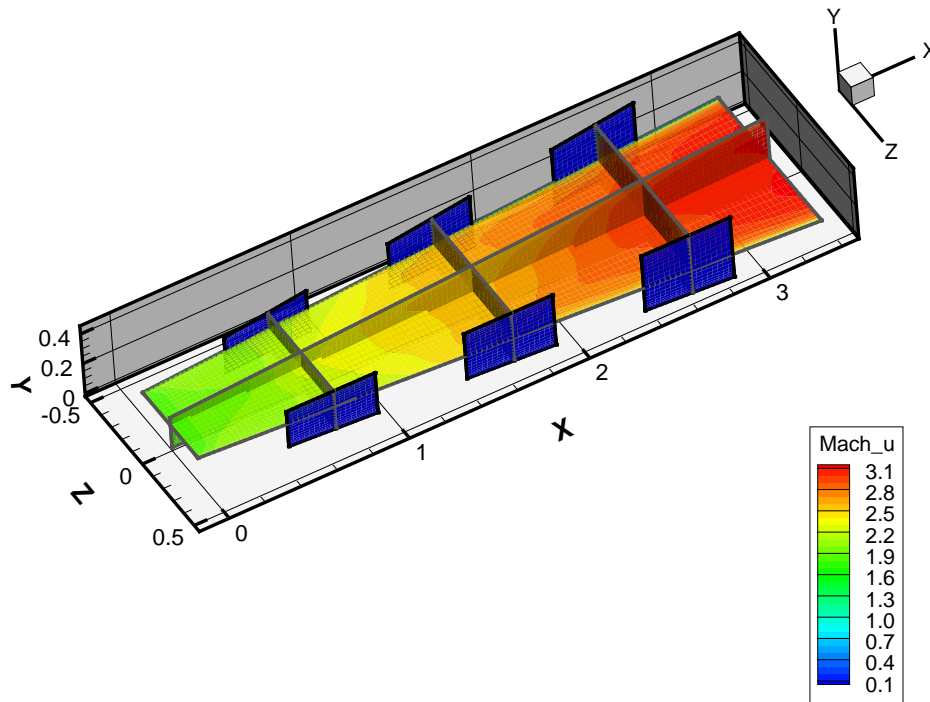


Figure 4.8 K16 Mach Number Contours

The electric field, created by the load factor $\mathcal{K} = 1.6$, is shown in Figure 4.9. This vector field shows how some of the field lines in the x-z midplane travel from one

set of electrodes to the next set of electrodes on the same wall. This is known as Hall effect which describes the phenomenon that charged particles, like electrons and ions, move in a perpendicular direction to an electric and magnetic field.[30] Also, leakage occurs on the inlet and exit of the nozzle. This is expected since there is no way to insulate the center of the flow field. The end of the x-y midplane shows how some of the vectors turn back into the nozzle.

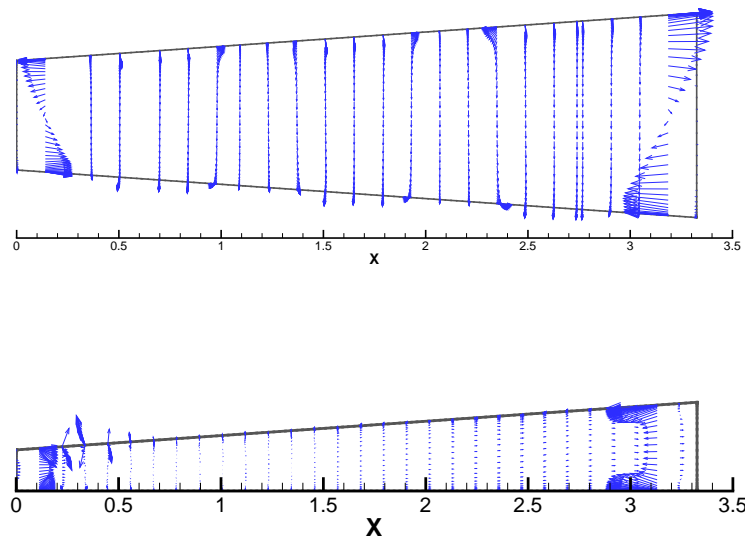


Figure 4.9 K16 Electric Field Vectors (top: x-z midplane, bottom: x-y midplane)

Figure 4.10 shows contours of the electric potential throughout the flow. It is interesting to note that the potential between the second and third set of electrodes along the walls is non-zero as if there were one big cathode and anode pair. It seems as if the electric field created by the electrodes may travel from the anode and cathode in the z-direction as well as to the adjacent electrode in the x-direction. The forward and reverse \vec{E} field vectors in Figure 4.9 support this explanation. This would also account for the Lorentz forces in the positive and negative z-directions that result fore and aft the electrodes in Figure 4.7. However, this result is more likely a combination of both the Hall effect and the bi-directional flow of the \vec{E} field.

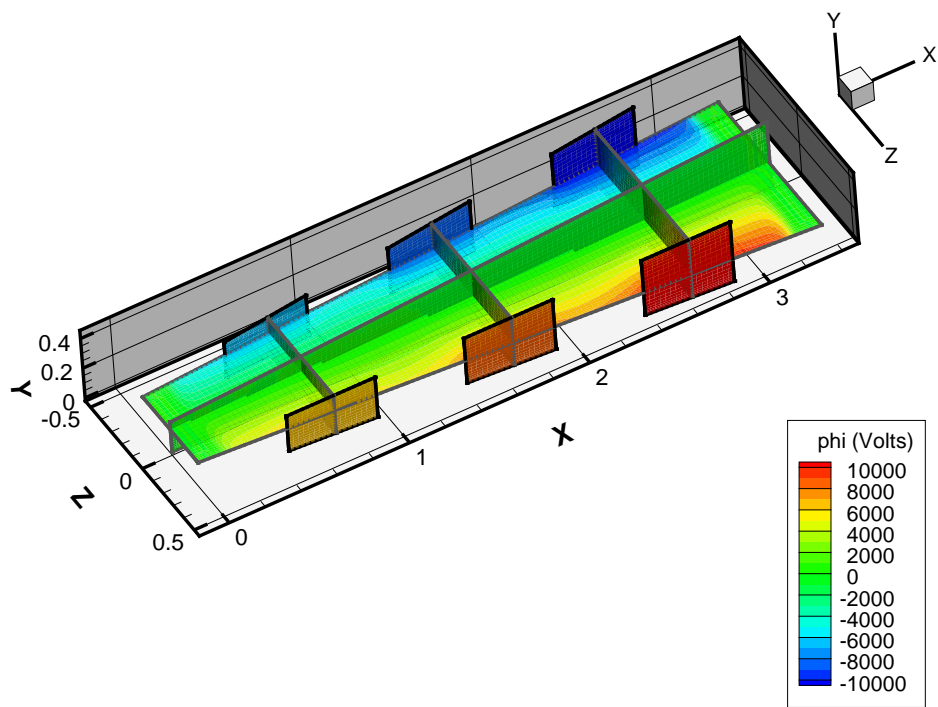


Figure 4.10 K16 Electric Potential Contours

A side effect of MGD acceleration is the increase in the temperature along the walls due to Joule heating. Figure 4.11 shows the temperature contours for the $\mathcal{K} = 1.6$. As expected, the temperature decreases in a diverging supersonic duct. However, the temperature increases by more than an order of magnitude along the walls with the electrodes. Figure 4.12 zooms in on the surface of the wall at the trailing edge of an electrode. Since the velocity is very slow and the electric potential is at its maximum at the electrodes, Joule heating causes abnormally large temperatures. In addition, these extremely high temperatures are probably also due to the type of boundary conditions enforced along the walls. More in depth analysis is needed on the proper type of boundary condition to employ.

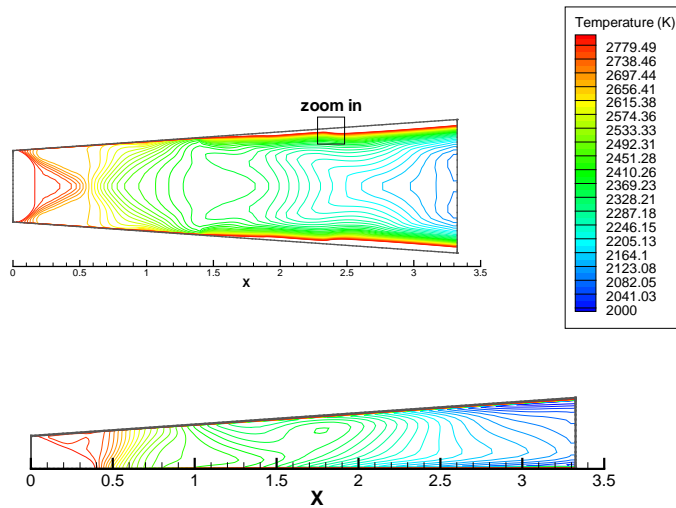


Figure 4.11 K16 Temperature (top: x-z midplane, bottom: x-y midplane)

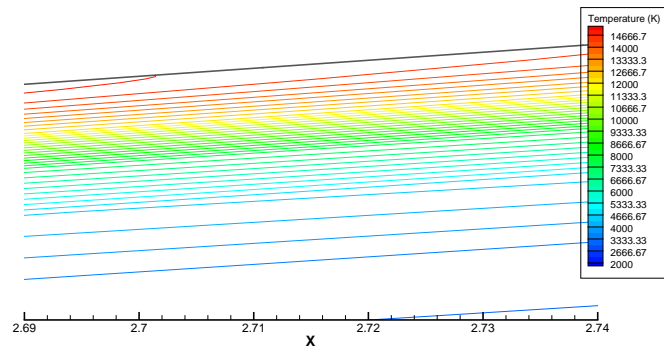


Figure 4.12 Close up of K16 Temperature

4.4 *Generation, $\mathcal{K} = 0.8$*

Flow field generation, or deceleration, occurs when the electric and magnetic fields are oriented such that the resulting Lorentz force decelerates the flow by pulling energy out of the flow field in the form of electric potential. Since the potential is kept constant on the electrodes, in a real life scenario, the resulting energy would be extracted as current. The K08, K09, K08_SIG2, and K09_SIG2 cases provided similar flow fields. As discussed in the previous section on specific thrust, the generation cases demonstrated some tendencies toward acceleration at the first electrode and reverted to the expected deceleration behavior at the following electrode due to the conductivity of the flow. The K08 case is discussed in this section. The rest of the MGD generation flow field plots can be found in Appendix A.

The Lorentz force field vectors for K08 case are shown in Figure 4.13. The largest deceleration force occurs at the second electrode. This happens because the load factor at the second electrode is artificially reduced by the acceleration at the first electrode and the conductivity is a maximum at the second electrode so the Lorentz force is very strong there. The third electrode shows a more moderate decelerating force on account of less conductivity at this electrode.

The Mach number contours are shown in Figure 4.14. The Mach number decreases between the second and third electrodes, and then increases before it reaches the exit plane. The second and third electrodes act like MGD generators, followed by a region of acceleration due to the nozzle geometry expansion. This can be confirmed by the absence of vectors behind the third electrode shown in Figure 4.13. This is also supported by the plot of specific thrusts shown in Figure 4.2.

Figure 4.15 shows the electrical field vectors. The electrical field around the first electrode looks similar to that of the K16 acceleration case as compared to Figure 4.2. There is a noticeable change in the vector field around the second and third electrodes: characterized by a reverse in the flow field direction which causes a decelerating Lorentz force.

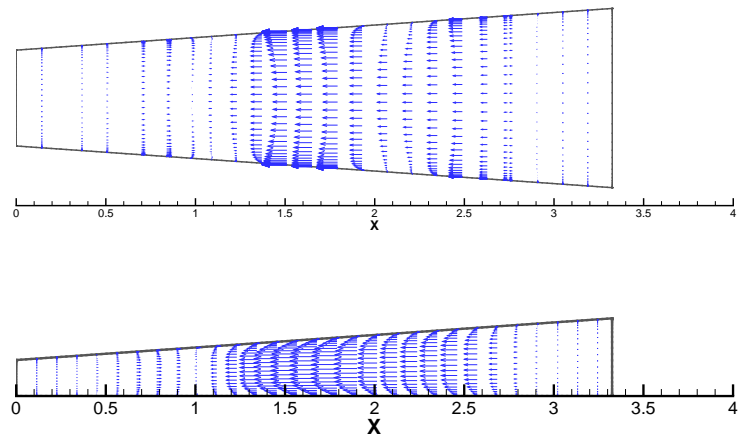


Figure 4.13 K08 Lorentz Force Vectors (top: x-z midplane, x-y midplane)

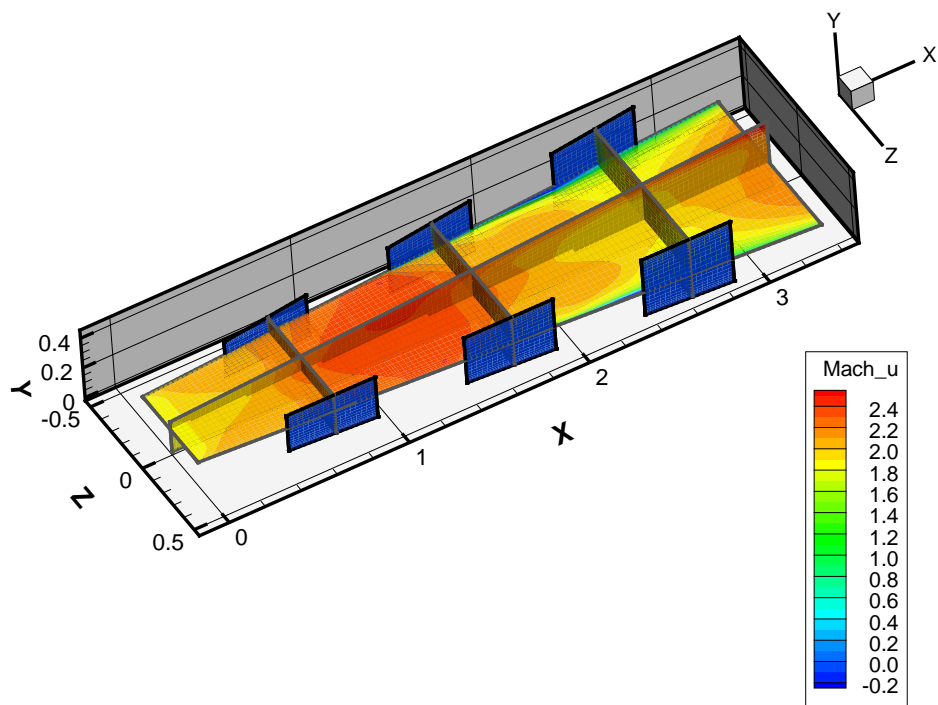


Figure 4.14 K08 Mach Number Contours

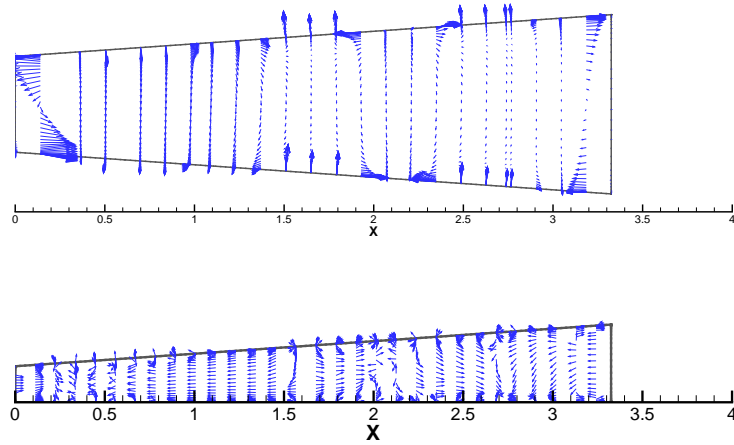


Figure 4.15 K08 Electrical Field Vectors (top: x-z midplane, x-y midplane)

The pressure contours are shown in Figure 4.16. The pocket of relatively lower pressure at the second set of electrodes is most likely caused by the interface between the acceleration and expected MGD generation. Over the later portion of the nozzle, the decrease in pressure is retarded, as expected, by the decelerating body forces.

The temperature contours are shown in Figure 4.17. It is interesting to note that the temperature is not as hot at the walls as in the K16 case. However, the temperature of the flow field in the middle of the nozzle is much hotter than that of the K16 case. This is due to the slowing down of the flow.

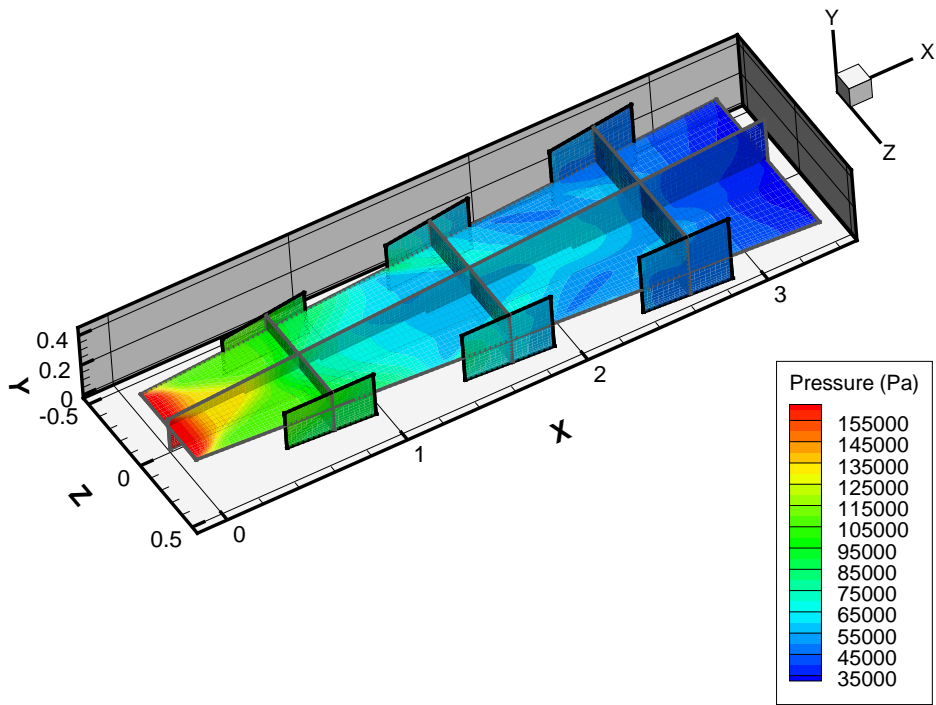


Figure 4.16 K08 Pressure Contours

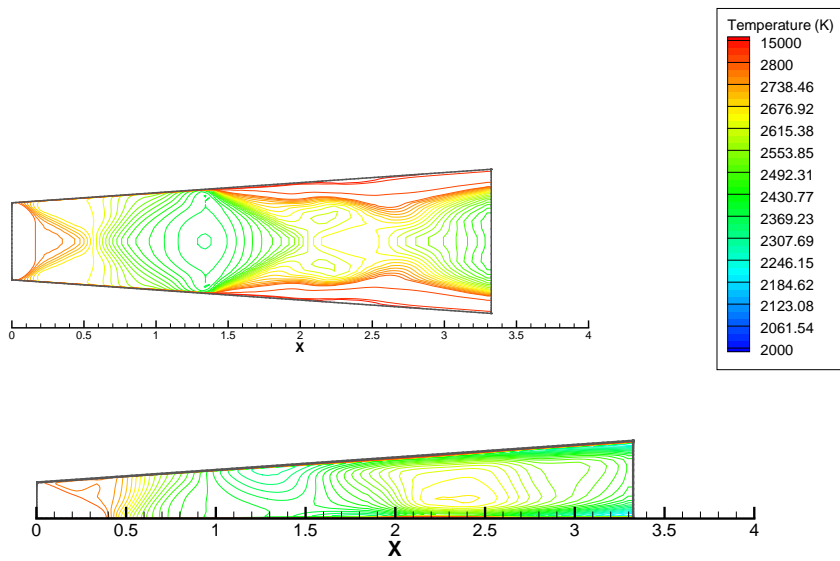


Figure 4.17 K08 Temperature Contours (top: x-z midplane, bottom: x-y midplane)

4.5 Efficiency

The efficiency results were determined using Eqn. 3.5 and Eqn. 3.7 by setting $P_{in\sigma}$ equal to zero. This method lead to skewed results on account of the electron beam power requirement not being included. These results are referred to as pseudo efficiencies since they do not include all of the power requirements. Figure 4.18 shows the pseudo efficiencies.

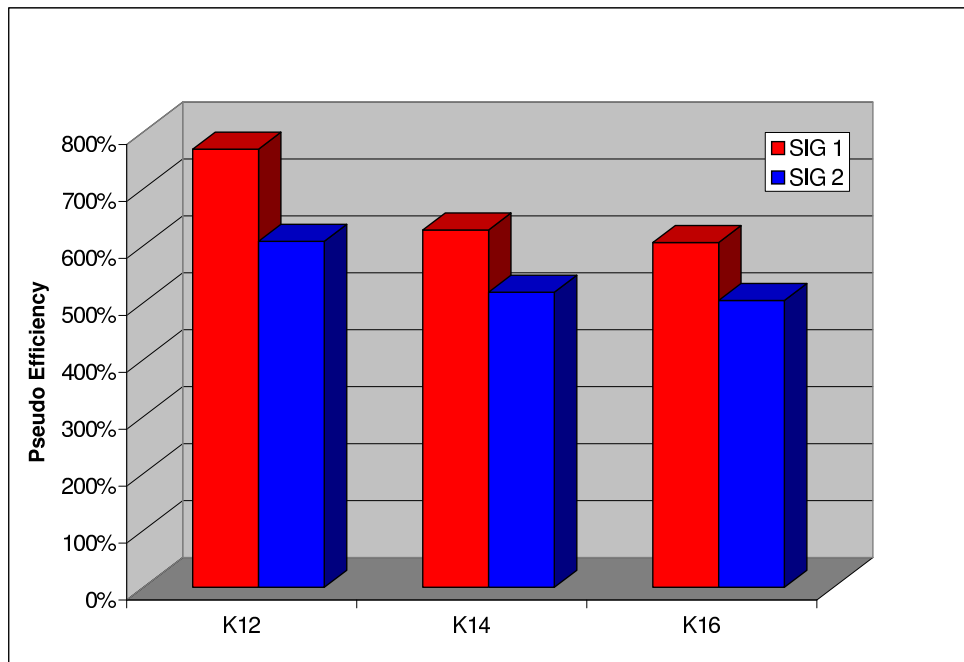


Figure 4.18 Accelerator Pseudo Efficiency

Given Eqn. 3.6 a greater specific thrust, $\frac{F}{\dot{m}}$, equates to a larger increase in power above that of the baseline case. As a result when electron beam requirements are neglected, it would be expected for the case with the largest specific thrust to also have the largest efficiency. However, this is not the case in Figure 4.18 in which the K16 case has the smallest pseudo efficiency. This is partly due to the fact that the voltage power requirements $P_{in\Delta\phi}$ was dwarfed by P_{out} for the lower load factors. It is also assumed that the power requirements for the conductivity pattern are the

dominant power requirements. This means that even an estimation of the efficiency would require the $P_{in\sigma}$ term in order to make sense.

In order to account for the effect that electron beam power requirements may have on the efficiency, a projected efficiency was calculated. Figure 4.19 shows the efficiency that would result given an arbitrary $P_{in\sigma}$. As expected, the projected efficiencies show that the higher specific thrust producing load factors have better efficiencies than the lower ones.

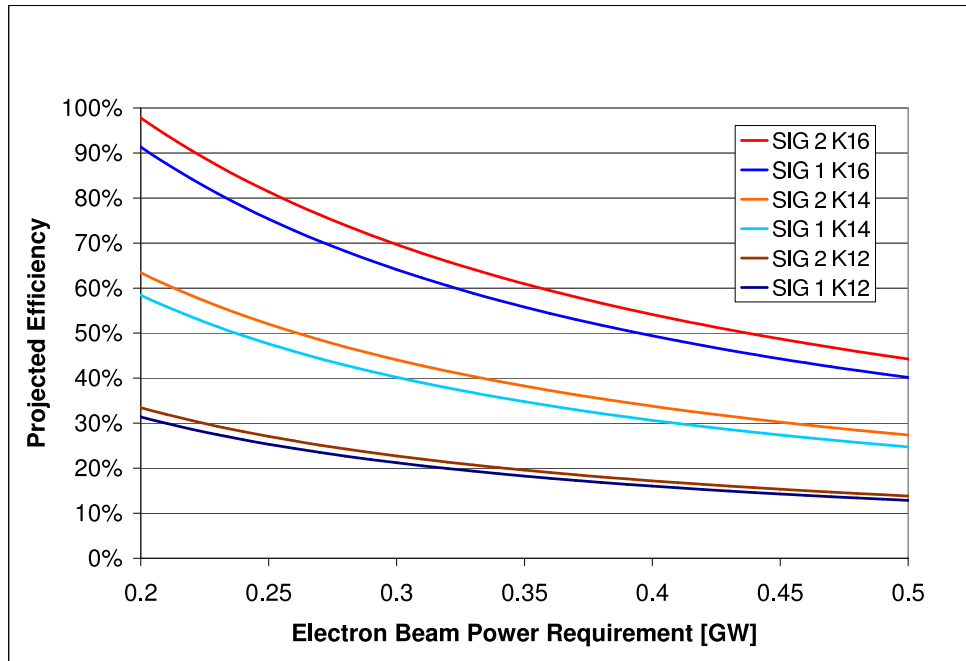


Figure 4.19 Accelerator Projected Efficiency

It is interesting to note that an optimistic efficiency of 97% results if the electron beam power requirement for the second conductivity pattern does not exceed 0.2 gigawatt when $\mathcal{K} = 1.6$. However, more research would have to be done on the power requirements for an electron beam capable of producing the conductivity pattern in this study. This leads to the notion that MGD acceleration can be a practical application, as long as the practical barriers such as material limitations are overcome.

5. Conclusions

5.1 *This Study*

The specific thrust, flow conditions, and efficiency results for the scramjet nozzle accelerator were examined computationally for a laminar flow with a free stream Mach number of 8. The changing parameters included load factors and conductivity patterns. The ultimate goal was to determine which parameters yielded the best performance in terms of specific thrust and efficiency.

The efficiency of the MGD acceleration could be reasonable if the electron beam ionization was added to the calculation. The pseudo efficiency results, ranging from a factor of 5.04 to 7.69, from this study only accounted for power requirements due to the electric potential requirements across the electrodes. Since the power requirements for electron beam ionization plays a significant role in efficiency, the pseudo efficiencies alone were not enough to draw conclusions. Figure 4.19 was created to project efficiencies that would result given possible electron beam power requirements. Given a beam ionization power requirement of 1 gigawatt or less, the efficiency of the $\mathcal{K} = 1.6$ case for SIG2 could yield decent results. However, more research would be needed to determine power requirements for each flow field.

A more definite performance measure used in this study was specific thrust. As shown in Table 4.1, specific thrust increased for the MGD acceleration cases, and decreased for the MGD deceleration cases. The second conductivity pattern with more ionization yielded more acceleration. The best acceleration was found for the $\mathcal{K} = 1.6$ case with the second conductivity pattern which had a 95% increase in specific thrust over the baseline.

More research should be done into deceleration load factors in the nozzle. The $\mathcal{K} = 0.9$ case for conductivity 2 yielded a -26% difference in specific thrust which fell outside of the trend considering that the $\mathcal{K} = 0.8$ only yielded a -23% difference. This may be due to the flow field decelerating enough to drift the load factor in Eqn. ??, which has the result of accelerating the flow. This effect may not have been

as noticeable in the SIG1 case simply because the conductivity decreased enough to have a only minute effect on the flow field when the load factor increased.

On a similar note, the initial acceleration at the first electrode for all the generation cases was due to the fact that the converged baseline case was used to determine the load factor, \mathcal{K} , at each electrode. The first electrode acted like an accelerator for all the cases. Then the flow shifted to generation as intended. Eqn. 4.1 accounts for this effect. The same principle has a similar effect on the acceleration cases. As the flow accelerated, the load factors at each successive electrode became less than intended. This had the effect of weaker increases in the stream thrust function, and ultimately less specific thrust.

In order to prevent the load factor drift, a controller should be implemented to vary the voltage with the reference velocity to regulate the change in load factor. In computational studies, this only means recalculating Eqn. 4.1 based on local parameters throughout each successive iteration. However, in real world applications, this would mean designing a control system with sensors capable of determining velocity of fluids without effecting the flow. Possible solutions could include lasers, or even feedback data from a power supply. Since the Lorentz force is a product of $\vec{j} \times \vec{B}$, and the load factor represents energy interaction with the electrodes, controlling the load factor could be achieved through the use of a current pumping power supply. Such power supplies are used in a variety of applications such as arc welding.

An increase in load factor had the effect of increasing both specific thrust and efficiency for each of the two conductivity patterns. The only drawback with increasing load factor is the addition of Joule heating at the electrodes. SIG2, the larger conductivity pattern, also yielded higher specific thrusts. However, efficiency conclusions could not be drawn concerning the change in conductivity pattern since the power requirements for conductivity were undetermined. MGD control may have a plausible future.

5.2 *Future Work*

The accuracy of the computational code when determining Joule heating at the walls remains uncertain. A study could be designed to test the limitations of the computational code. It might be interesting to find if there are certain load factors that cause problems.

More investigation could also be done into the efficiency of the generating conditions. Macheret *et al.* of Princeton university developed a method of determining efficiency of the generator using computational parameters[23]. He also designed a computational study that may have been more efficient by placing small scale, on the order of millimeters, electron beam windows directly in front of each of ten electrodes. It might be interesting to compare the ionization results of this study to those of Macheret *et al.*. Their study had efficiencies on the order of 13% with electron beam power requirements of 8.72 kilowatts[23]. Since this study is on a completely different scale, comparison of those results is not possible. However, it would be interesting to set up a computational experiment that could compare the two methods.

Appendix A. Other Cases

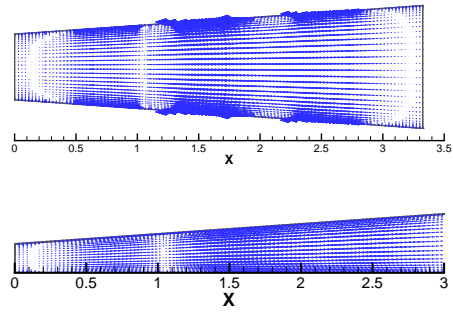


Figure A.1 K09 $\vec{j} \times \vec{B}$

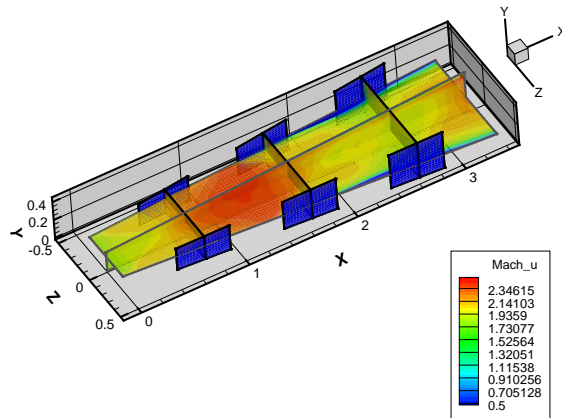


Figure A.2 K09 Mach Number

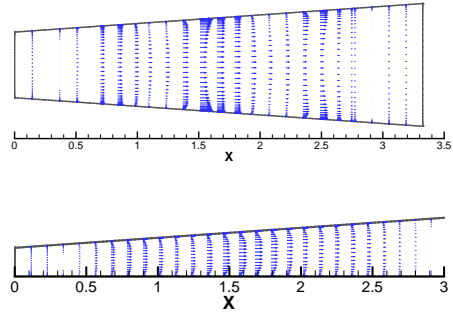


Figure A.3 $K12 \vec{j} \times \vec{B}$

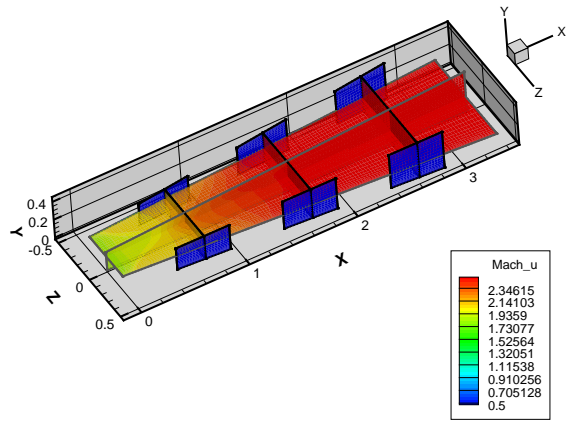


Figure A.4 K12 Mach Number

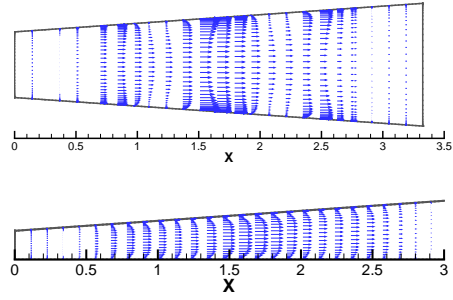


Figure A.5 K14 $\vec{j} \times \vec{B}$

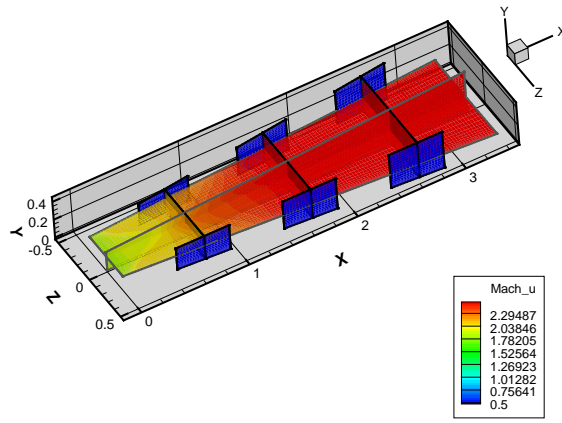


Figure A.6 K14 Mach Number

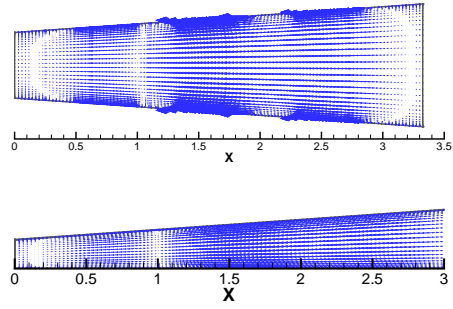


Figure A.7 K08_SIG2 $\vec{j} \times \vec{B}$

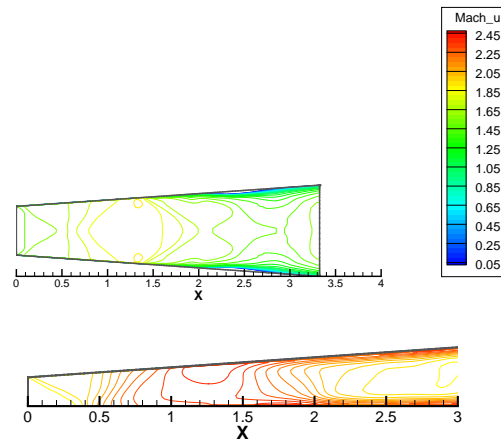


Figure A.8 K08_SIG2 Mach Number

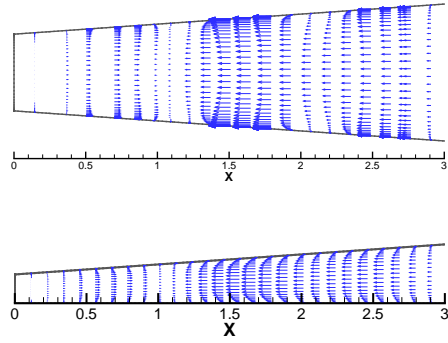


Figure A.9 K09_SIG2 $\vec{j} \times \vec{B}$

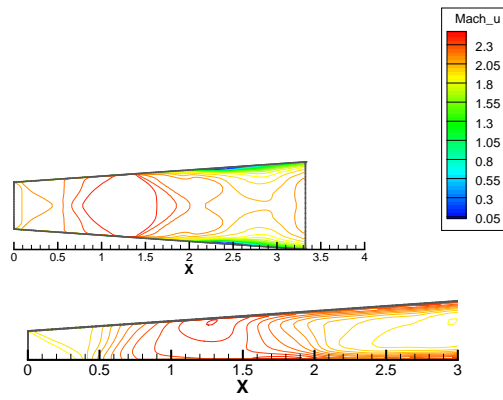


Figure A.10 K09_SIG2 Mach Number

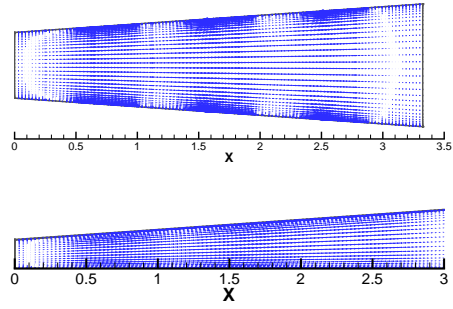


Figure A.11 $K12_SIG2 \vec{j} \times \vec{B}$

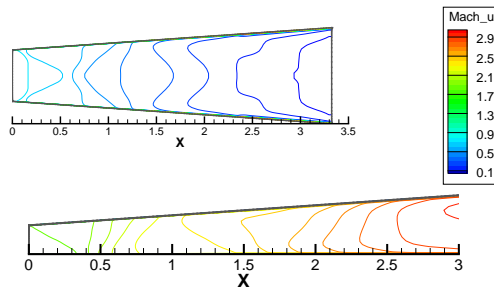


Figure A.12 $K12_SIG2$ Mach Number

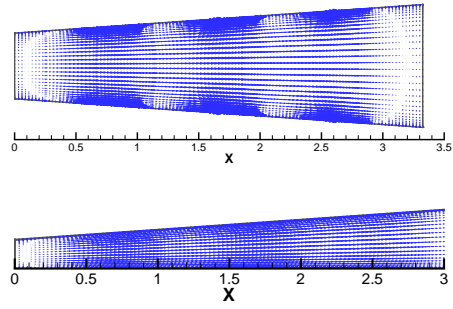


Figure A.13 K14.SIG2 $\vec{j} \times \vec{B}$

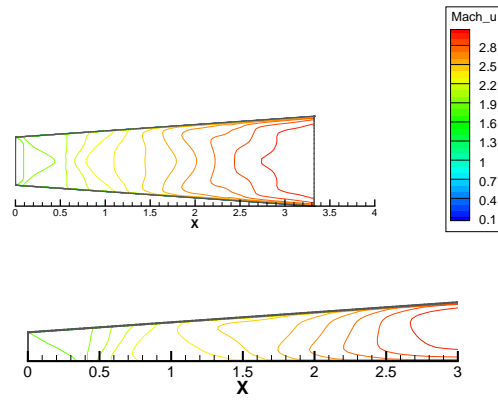


Figure A.14 K14.SIG2 Mach Number

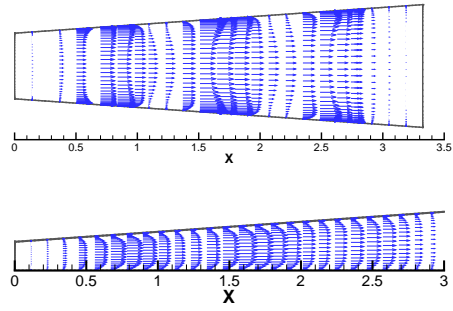


Figure A.15 K16_SIG2 $\vec{j} \times \vec{B}$

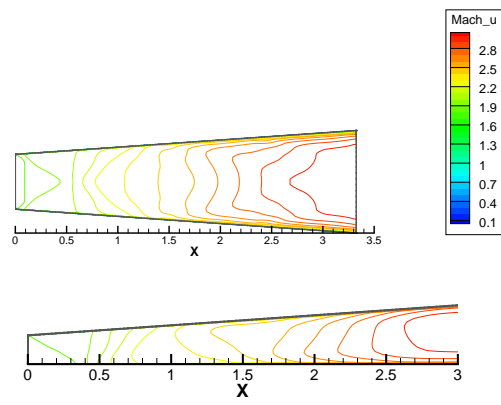


Figure A.16 K16_SIG2 Mach Number

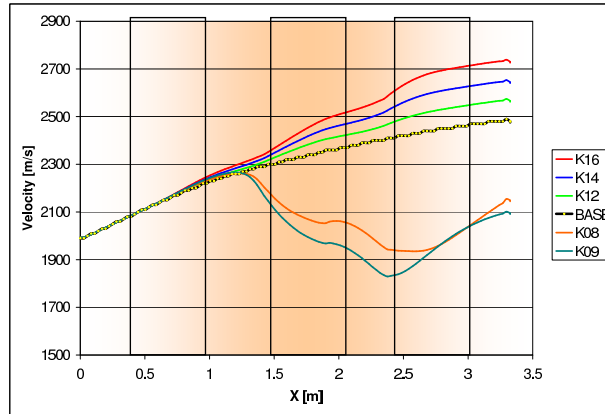


Figure A.17 SIG1 Velocity

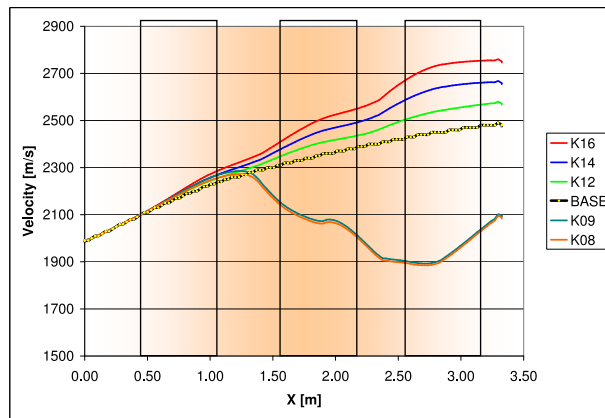


Figure A.18 SIG2 Velocity

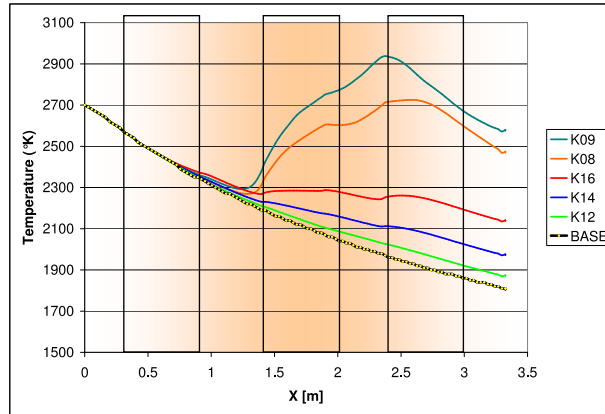


Figure A.19 SIG1 Temperature

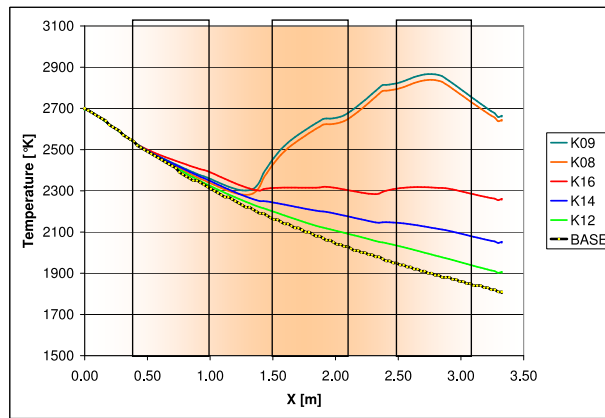


Figure A.20 SIG2 Temperature

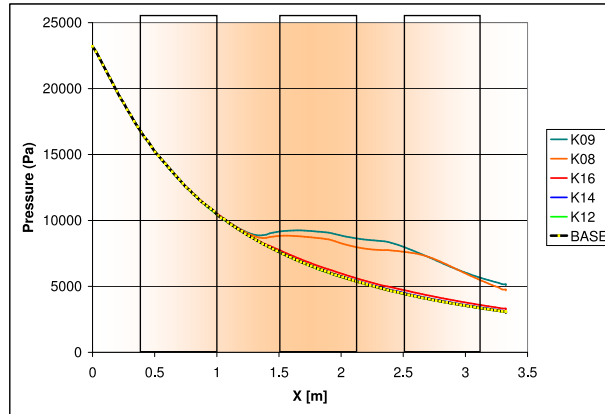


Figure A.21 SIG1 Pressure

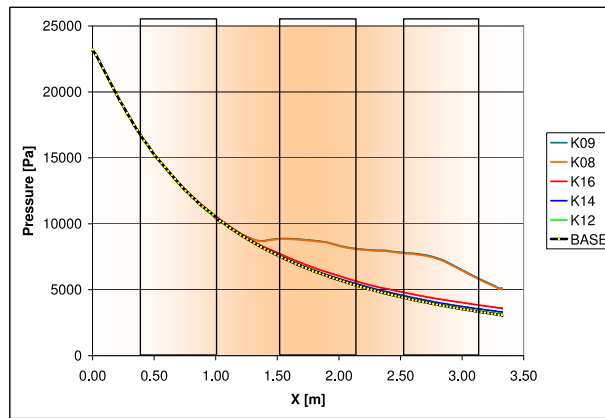


Figure A.22 SIG2 Pressure

Bibliography

1. “Personal Corespondence with M. Lindsey,” 2004-5.
2. Anderson, J. D. *Hypersonics and High Temperature Gas Dynamics*. Reston, VA: AIAA, 2000.
3. Ardelyan, N., et al. *Modeling of Plasmas in Electron Beams and Plasma Jets for Aerodynamic Applications*. AIAA Paper 2001–3101, June 2001.
4. Bityurin, V. A. and A. N. Bocharov. *Results of Experiments on MHD Hypersonic Flow Control*. AIAA Paper 2004–2263, June 2004.
5. Chapman, Stephen J. *Fortran 90/95 for Scientists and Engineers*. Boston, MA: McGraw-Hill, 1998.
6. Dugdale, D. *Essentials of Electromagnetism*. New York: American Institute of Physics, 1993.
7. Earp, B. E. *Magnetogasdynamic Flow Control of a Mach Reflection*. MS thesis, Airforce Institute of Tecnology, WPAFB, OH, March 2004.
8. Einstein, A. *Relativity, The Special and General Theory*. Three Rivers Press, 1961.
9. “Ramjet, Scramjet, and PDE,” *Ramjet, Scramjet, and PDE* Paul Kuentzmann Website, (2005). 24 May 2005 <http://www.onera.fr/conferences/ramjet-scrumjet-pde/>.
10. Gaitonde, D. V. *Three-Dimensional Flow-Through Scramjet Simulation with MGD Energy- Bypass*. AIAA Paper 2003–0172, Jan 2003.
11. Gaitonde, D. V. and J. Poggie. *Simulation of Magnetogasdynamic Flow Control Techniques*. AIAA Paper 2000–2326, Jun 2000.
12. Gaitonde, D. V. and J. Poggie. *An Implicit Technique for 3-D Turbulent MGD with the Generalized Ohms Law*. AIAA Paper 2001–2736, Jun 2001.
13. Gaitonde, D. V. and J. Poggie. *Elements of a Numerical Procedure for 3-D MGD Flow Control Analysis*. AIAA Paper 2002–0198, Jan 2002.
14. Gaitonde, D. V. and J. Poggie. *Preliminary Analysis of 3-D Scramjet Flowpath with MGD Control*. AIAA Paper 2002–2134, May 2002.
15. Gaitonde, Datta V. “Higher-Order Solution Procedure for Three-Dimensional Nonideal Magnetogasdynamics,” *AIAA Journal*, 39(11):2111–2119 (November 2001).
16. Harrington, B. H. *Magnetogasdynamic Flow Acceleration in a SCRAMJET Noz-zle*. MS thesis, Airforce Institute of Tecnology, WPAFB, OH, June 2004.

17. Heiser, W.H. and D.T. Pratt. *Hypersonic Airbreathing Propulsion*. Washington, DC: American Institute of Aeronautics and Astronautics, 1994.
18. Hughes, W. F. and F. J. Young. *The Electromagnetodynamics of Fluids* (Reprint Edition). Malabar, FL: Robert E. Krieger Publishing Company, 1989.
19. “HyShot Breath into Space,” *Hypersonics Research Speeds Up* HyShot Website, (2004). 24 May 2005 <http://www.hyshot.info/modules.phpnameNewsfile=articlesid=3>.
20. “HyShot Breathe into Space,” *UQ puts the wind up US* in HyShot Website, (2005). 24 May 2005 <http://www.hyshot.info/modules.phpnameNewsfile=articlesid=17>.
21. Macheret, S. O., et al. *Electron Beam Generated Plasmas in Hypersonic MHD Channels*. AIAA Paper 99–3635, June 1999.
22. Macheret, S. O., et al. *Optimum Performance of Electron Beam Driven MHD Generators for Scramjet Inlet Control*. AIAA Paper 2003–3763, June 2003.
23. Macheret, S.O., et al. *Electron Beam Generated Plasmas in Hypersonic MHD Channels*. AIAA Paper 99–3635, June 1999.
24. Mehta, U. B., et al. *A Perspective on a Combined Magneto-Hydrodynamic-Scramjet Engine*. ISABE Paper 2001–1231, Sep 2001.
25. “NASA’s X-43A Scramjet Breaks Speed Record,” May 2005. http://www.nasa.gov/home/hqnews/2004/nov/HQ_04373_x43a_scramjet.html.
26. “Sam Barros’ PowerLabs,” May 2005. <http://www.powerlabs.org/>.
27. Poggie, J. and D. V. Gaitonde. *Simulation of MHD Flow Control Techniques*. AIAA Paper 2000–2326, June 2000.
28. Poggie, J. and D. V. Gaitonde. *Computational Studies of Magnetic Control in Hypersonic Flow*. AIAA Paper 2001–0196, January 2001.
29. Poggie, J. and D. V. Gaitonde. *Electrode Boundary Conditions in Magnetogasdynamic Flow Control*. AIAA Paper 2002–0199, January 2002.
30. Serway, R. and R. Beichner. *Physics For Scientists and Engineers*. Orlando, FL: Saunders College Publishing, 2000.
31. Vatazhin, A.B. and V.I. Kopchenov. *Problem of Hypersonic Flow Deceleration by Magnetic Field*. Washington, DC: American Institute of Aeronautics and Astronautics, 2000.
32. Versteeg, H. K. and W. Malalasekera. *An Introduction to Computational Fluid Dynamics*. Pearson Prentice Hall, 1995.
33. “Men of the X-1,” *Faster Than Sound* NOVA online Website, (1997). 29 Apr 2005 <http://www.pbs.org/wgbh/nova/barrier/men.html>.
34. “Scramjet experiment soars off California coast.” *Spaceflight Now* Spaceflight Now Website, (2004). 21 Apr 2005 <http://www.spaceflightnow.com/news/n0403/27x43a/>.

Vita

Ensign Erik K. Ross was born in Rockport, ME. He was raised on Cape Cod, MA, and graduated from Falmouth High School in 2000. He spent a year at Providence College in Providence, RI, when he decided that he wanted to join the Navy. He transferred to Worcester Polytechnic Institute in Worcester, MA, where he graduated with a Bachelor of Science degree in Mechanical Engineering and was commissioned in May of 2004.

In June 2004, he entered the Aeronautical Engineering program at the Graduate School of Engineering and Management, Air Force Institute of Technology. Upon graduation, he will be assigned to the Aviation Pre-flight Indoctrination program at NAS Pensacola, FL, where he will begin training to become a Naval Aviator.

Permanent address: 2950 Hobson Way
WPAFB, Ohio 45433-7765

REPORT DOCUMENTATION PAGE

Form Approved
OMB No. 0704-0188

The public reporting burden for this collection of information is estimated to average 1 hour per response, including the time for reviewing instructions, searching existing data sources, gathering and maintaining the data needed, and completing and reviewing the collection of information. Send comments regarding this burden estimate or any other aspect of this collection of information, including suggestions for reducing this burden to Department of Defense, Washington Headquarters Services, Directorate for Information Operations and Reports (0704-0188), 1215 Jefferson Davis Highway, Suite 1204, Arlington, VA 22202-4302. Respondents should be aware that notwithstanding any other provision of law, no person shall be subject to any penalty for failing to comply with a collection of information if it does not display a currently valid OMB control number. PLEASE DO NOT RETURN YOUR FORM TO THE ABOVE ADDRESS.

1. REPORT DATE (DD-MM-YYYY) 13-06-2005		2. REPORT TYPE Master's Thesis		3. DATES COVERED (From — To) Jul 2004 – Jun 2005	
4. TITLE AND SUBTITLE Study of Magnetogasdynamic Flow Acceleration in a Scramjet Nozzle				5a. CONTRACT NUMBER	
				5b. GRANT NUMBER	
				5c. PROGRAM ELEMENT NUMBER	
6. AUTHOR(S) Ross, Erik K., Ensign, USN				5d. PROJECT NUMBER 2003-014	
				5e. TASK NUMBER	
				5f. WORK UNIT NUMBER	
7. PERFORMING ORGANIZATION NAME(S) AND ADDRESS(ES) Air Force Institute of Technology Graduate School of Engineering and Management 2950 Hobson Way WPAFB OH 45433-7765				8. PERFORMING ORGANIZATION REPORT NUMBER AFIT/GAE/ENY/05-J11	
9. SPONSORING / MONITORING AGENCY NAME(S) AND ADDRESS(ES) AFOSR/NA Dr. John Schmisser 875 N. Randolph Street, Suite 325, Rm 3112 Arlington VA 22203-1977 (703) 696-6962				10. SPONSOR/MONITOR'S ACRONYM(S)	
				11. SPONSOR/MONITOR'S REPORT NUMBER(S)	
12. DISTRIBUTION / AVAILABILITY STATEMENT Approval for public release; distribution is unlimited.					
13. SUPPLEMENTARY NOTES					
14. ABSTRACT The research project studied the benefits of Magnetogasdynamic (MGD) acceleration on a scramjet nozzle. MGD is a technology that relies on electromagnetic fields to extract and/or add energy to flow fields. The scramjet engine in the "AJAX" concept proposed by D.I.Brichkii et al. (2001) of St. Petersburg, Russia would utilize an MGD power generator in the diffuser which could potentially provide electrical power for the aircraft support systems and an MGD accelerator in the nozzle of the engine. Using an AFRL/VAAC CFD code that was modified for MGD computations, this project investigated the effect conductivity and load factor had on the specific thrust and efficiency of an MGD accelerator composed of segmented electrodes in the nozzle of a scramjet engine. For a load factor of 1.6, results showed a 95% increase in specific thrust. When MGD generation was employed at a load factor of 0.8, a 31% decrease in specific thrust was calculated. The solutions included high wall temperatures which need more investigation for MGD acceleration to be practical.					
15. SUBJECT TERMS Magnetogasdynamics; Flow Control; Flow Acceleration; Scramjet Nozzle; MGD Accelerator; Plasma					
16. SECURITY CLASSIFICATION OF:			17. LIMITATION OF ABSTRACT	18. NUMBER OF PAGES	19a. NAME OF RESPONSIBLE PERSON
a. REPORT	b. ABSTRACT	c. THIS PAGE			Richard J. McMullan, Maj, USAF (ENY)
U	U	U	UU	81	19b. TELEPHONE NUMBER (include area code) (937)255-3069, Richard.Mcmullan@afit.edu